communications medicine

A Nature Portfolio journal

Article

https://doi.org/10.1038/s43856-026-01528-3

The 5-HT1A receptor antagonist WAY-100635 maleate promotes retinal ganglion cell differentiation and protects the retino-visual circuits

Sayanta Dutta[1], Michelle L. Surma[1], Jie Chen[2], Kavitha Anbarasu[1,3], Jingwei Meng[4], Nian Wang[2,5,6] & Arupratan Das[1,3,4,7]

Abstract

Background Growing evidence implicates early metabolic dysfunctions in retinal ganglion cells (RGCs) as a contributor to both high- and normal-tension glaucoma, yet no approved therapy directly protects RGCs to preserve vision. We aimed at identifying a safe, druggable neuroprotective strategy that restores RGC metabolic homeostasis for glaucoma therapy.
Methods Using a live-cell mitochondrial screen in human embryonic stem cell-derived retinal ganglion cells (H7; female donor), we identified the clinically tested 5-HT1A antagonist WAY-100635 (WAY) as a neuroprotective agent. Mechanisms are probed by pharmacologic competition with agonist 8-OH-DPAT, cAMP assays, and PGC-1α dependent mitochondrial-biogenesis tests. RGC metabolism and survival are assessed by Seahorse and apoptosis assays. In vivo efficacy is evaluated in acute optic-nerve crush (ONC) and microbead-induced ocular-hypertension glaucoma models using histology, brain MRI, visual-acuity, contrast sensitivity testing, and flash VEPs to quantify cortical responses in wild-type C57BL/6 J male mice. Statistics used two-tailed Student's t-tests or ANOVA, as appropriate.
Results Here we show that WAY elicits a reversible cAMP surge that drives PGC-1α dependent mitochondrial biogenesis and reduces apoptosis in hRGCs. In glaucoma-associated OPTN^{E50K} hRGCs, it restores mitochondrial fitness, attenuates excitotoxicity, and shifts metabolism toward aerobic glycolysis, while in progenitors, WAY enhances cristae maturation, oxidative phosphorylation, accelerating RGC specification. Systemic dosing in ONC mice preserves RGC somata, retinal function (PhNR), and optic-pathway integrity. WAY-treated glaucoma mice show preserved visual acuity and fVEP propagation to cortex, halting glaucoma progression.
Conclusions A clinically tested 5-HT1A antagonist WAY restores RGC metabolic homeostasis and preserves visual-pathway function across acute and chronic injury models, without detected systemic toxicity, supporting development of a neuroprotective candidate for glaucoma and potentially for other mitochondrial optic neuropathies.

Plain Language Summary

Glaucoma slowly damages the nerve cells called retinal ganglion cells (RGCs) that carry signals from the eye to the brain. Current treatments mainly lower eye pressure but even when treated, many patients continue to lose vision. We screened for various possible compounds on human RGCs and discovered a drug already tested in people for another reason keeps RGCs alive during optic nerve injury and maintains the ability for visual signals to move from the eye to the brain, including in conditions where glaucoma develops. These results suggest this treatment could be used alongside pressure-lowering treatments to preserve vision. Further testing is needed to check this would be suitable for people with glaucoma.

[1]Department of Ophthalmology, Eugene and Marilyn Glick Eye Institute, Indiana University School of Medicine, Indianapolis, IN, USA. [2]Advanced Imaging Research Center, The University of Texas Southwestern Medical Center, Dallas, TX, USA. [3]Department of Medical and Molecular Genetics, Indiana University School of Medicine, Indianapolis, IN, USA. [4]Department of Biochemistry and Molecular Biology, Indiana University School of Medicine, Indianapolis, IN, USA. [5]Department of Biomedical Engineering, University of Texas Southwestern Medical Center, Dallas, TX, USA. [6]Peter O'Donnell Jr. Brain Institute, University of Texas Southwestern Medical Center, Dallas, TX, USA. [7]Stark Neurosciences Research Institute, Indiana University School of Medicine, Indianapolis, IN, USA.
e-mail: arupdas@iu.edu

Neurons with long axons and partial unmyelination are particularly susceptible to mitochondrial dysfunctions. Retinal ganglion cells (RGCs) remain unmyelinated in the retina through the posterior end of lamina cribrosa, which lacks saltatory conduction and relies on densely packed mitochondria for efficient action potential propagation and transport, requiring a high level of adenosine triphosphate (ATP)[1,2]. RGC degeneration stemming from mitochondrial abnormalities is a defining feature of both glaucoma and mitochondrial optic neuropathies (MON), including Leber hereditary optic neuropathy (LHON) and dominant optic atrophy (DOA)[2].

While elevated intraocular pressure (IOP) has traditionally been regarded as the hallmark of glaucoma, ~40–50% of patients still experience progressive vision loss despite well-controlled IOP[3]. Moreover, a significant primary open-angle glaucoma (POAG) patients present with RGC and vision loss in the context of normal IOP, often referred to as normal tension glaucoma (NTG)[4]. These clinical findings highlight the urgent need for therapeutic approaches that go beyond IOP management. Glaucoma is widely considered axogenic, with early deficits in anterograde transport and distal axonopathy, most prominently at the optic nerve head preceding soma loss; thus, interventions that preserve or restore axonal function may help halt disease progression[5]. This has been shown in glaucoma models where increased IOP disrupts mitochondrial function[6] and depletes ATP[7], impairing axonal transport and ultimately leading to RGC death[5,8,9].

Mitochondrial dysfunction is increasingly recognized as a fulcrum of RGC degeneration, making mitochondrial repair an attractive therapeutic entry point. Genetic strategies that enforce mitochondrial fusion[10] or boost anterograde transport by over-expressing Armcx1[11], Disc1[12], or the Optineurin (OPTN) associated TRAK1-KIF5B motor complex[13], drive impressive RGC axon regrowth in the optic nerve after optic-nerve crush (ONC). Likewise, metabolic augmentation with pyruvate[14], nicotinamide/Vitamin B_3, NAD^+, or Nmnat1 gene therapy[15,16] attenuates RGC loss in models of elevated IOP. However, chronic mitochondrial fusion or relentless distal transport can disrupt healthy dynamics and deplete mitochondria in the proximal axonal regions, while sustained oxidative phosphorylation (OXPHOS) by mitochondria risks toxic oxidative by-products, limiting the long-term benefit. Most importantly, no current intervention has restored functional eye-to-brain connectivity, which is a prerequisite for glaucoma therapy. A non-invasive, metabolism-restorative small molecule capable of rebuilding the retino-visual pathway would therefore constitute a transformative leap toward durable neuroprotection in glaucoma.

Here, we combined phenotypic screening with human stem-cell-derived retinal ganglion cells (hRGCs) to pinpoint small molecules that restore mitochondrial fitness. The screen revealed WAY-100635 maleate (WAY), a well-studied 5-HT1A Gi/o-coupled receptor antagonist[17,18], as a potent, reversible inducer of cyclic AMP and PGC-1a-driven mitochondrial biogenesis. WAY confers metabolic reprogramming that accelerates hRGC differentiation and grants strong neuroprotection to hRGCs harboring the glaucoma-linked $OPTN^{E50K}$ mutation[19]. The $OPTN^{E50K}$ mutation is found among a severe form of NTG patients characterized by defective mitochondrial homeostasis[19,20]. In vivo, a systemic course of WAY preserves RGC somata, protects axons through the optic nerve and central visual targets after crush injury, and safeguards both RGC survival, optic nerve function and visual acuity in glaucoma models. Crucially, WAY has already cleared FDA toxicology hurdles as a serotonin-receptor probe in clinical trials (NCT00603018, NCT02810717), streamlining its path toward clinical deployment.

Collectively, our data establish a pharmacologic blueprint for protecting long-distance RGC axons capable of delivering visual stimuli to the brain without the constitutive changes or delivery barriers of gene therapy. Because mitochondrial failure is a shared lesion across neurodegenerative disorders, this strategy may extend to Parkinson's disease, amyotrophic lateral sclerosis, and beyond, expediting translation through repurposing of a drug with an established safety record.

Methods

Reagents and software used in this study are listed in Supplementary Table S1.

ESC maintenance

Human embryonic stem cells (H7-hESCs; WiCell, Madison, WI) were used as the retinal ganglion cell (RGC) reporter line. The H7-hESC line is an NIH-registered human embryonic stem cell line (NIH Registration No. 0061; female donor). These cells were genetically modified via CRISPR/Cas9 to insert a multicistronic BRN3B-P2A-tdTomato-P2A-Thy1.2 construct into the endogenous BRN3B locus, enabling selective fluorescent labeling and surface tagging of RGCs as an isogenic reporter system[21]. A second CRISPR-engineered reporter line [H7-hESC ($OPTN^{E50K}$)] carrying the glaucoma-associated E50K mutation in the OPTN gene was previously described and used by us for disease modeling[20]. All hESC lines were maintained in mTeSR1 medium (STEMCELL Technologies) on Matrigel-coated plates at 37 °C in a humidified incubator with 5% CO_2. Routine passaging was performed using Gentle Cell Dissociation Reagent (STEMCELL Technologies) when cultures reached 70–80% confluency. Briefly, media were aspirated, cells were incubated with Gentle Dissociation Reagent for 5 min, and colonies were dissociated into small clumps via gentle trituration in fresh mTeSR1 before being reseeded onto new Matrigel-coated plates.

hRGC differentiation and immunopurification

Stem cell colonies were dissociated into single cells using Accutase (Sigma) for 10 min at 37 °C. Enzymatic activity was quenched by adding an equal volume of mTeSR1 medium (mT) supplemented with 5 μM blebbistatin (blebb). The cells were then centrifuged at 150 × *g* for 6 min, resuspended in mT containing 5 μM blebb, and counted using a hemocytometer. A total of 100,000 cells were plated per well of a Matrigel-coated 24-well plate. After 24 h, the medium was replaced with fresh mT lacking blebbistatin. Another 24 h later, the culture medium was switched to induction neural specification (iNS) medium, and directed differentiation toward retinal ganglion cells (hRGCs), which was initiated using a small molecule-based protocol as previously described[22]. Differentiation was monitored by expression of the tdTomato reporter under the BRN3B promoter. Between days 45 and 55, $tdTomato^+$ hRGCs were enriched using anti-THY1.2 microbeads and magnetic-activated cell sorting (MACS; Miltenyi Biotec), following previously established procedures[21,22]. Purified hRGCs were resuspended in iNS medium, counted, and plated onto Matrigel-coated coverslips, plates, or MatTek dishes for downstream analyses.

To enhance hRGC differentiation, cultures were treated with WAY-100635 at various time points and doses, as indicated in Fig. 5a–c and Supplementary Fig. 3a–c. Live cell fluorescence images of tdTomato-positive cells were captured on day 32 of differentiation using a Nikon EVOS microscope equipped with a 10×/0.25 NA objective. Following imaging, cells were collected for flow cytometric analysis to quantify the percentage of tdTomato-positive cells, representing the differentiated hRGCs.

Small molecule screening

Cold Matrigel (30 μl) was dispensed into each well of a 384-well plate using a Thermo Scientific Multidrop 384 and incubated overnight at 37 °C in 5% CO_2 to allow for gelation. The following day, excess Matrigel was removed by inverting the plate onto paper towels, and 50 μl of a cell suspension containing 10,000 hRGCs in iNS medium was added to each well. After a 48-h incubation, media was aspirated using an automated vacuum system, and cells were labeled with 50 μl iNS medium containing 10 nM MitoTracker Deep Red (MTDR) for 15 minutes. Drug compounds were then dispensed using a Tecan EVO100 with a PIN tool, delivering 0.25 μl from a 1 mM stock plate to achieve a final concentration of 5 μM, and the cells were incubated for an additional 24 h. Subsequently, the media was aspirated using an automated vacuum, and cells were treated with 15 μl Accutase per well for 20 min at 37 °C. To each well, 50 μl of iNS medium was added, and the cell suspension was mixed thoroughly by pipetting. The resulting single-cell

suspensions were transferred using a Tecan EVO150 MCA with disposable tips into a 384-well U-bottom plate. Plates were then analyzed on a Thermo Fisher Attune NxT flow cytometer equipped with an autosampler, and MTDR fluorescence intensity was quantified to assess mitochondrial content across drug-treated conditions relative to DMSO controls.

Mitochondrial mass measurement by Flow cytometry

Purified hRGCs were seeded at a density of 30,000 cells per well in Matrigel-coated 96-well plates and cultured for 3 days in iNS medium. To assess mitochondrial mass, cells were first labeled with MitoTracker Deep Red (MTDR), a mitochondrial membrane potential-sensitive live cell dye. Following MTDR labeling, hRGCs were treated with WAY-100635 at various time points. At the end of each treatment, cells were dissociated into single-cell suspensions using Accutase, and mitochondrial content was quantified using a Thermo Fisher Attune NxT flow cytometer. Fluorescence intensity from far-red channel (MTDR) was used as a direct readout for average mitochondrial mass in individual cell.

Cell viability and caspase activity

Stem cell differentiated hRGCs were plated at a density of 25,000 cells per well in 96-well clear-bottom, black-walled plates and cultured for 3 days. Subsequently, cells were treated with WAY, DPAT, or WAY with or without PGC1α targeted and non-targeted ASO at specified time points. Caspase activity was assessed using the ApoTox-Glo Triplex assay kit (Promega). For this, 100 µl of Caspase-Glo® 3/7 reagent was added to each well, and the plate was incubated for 30 min at room temperature. Luminescence was then recorded to quantify caspase activity. All caspase measurements were normalized to the corresponding control condition.

Immunofluorescence and confocal imaging

Purified stem cell-derived human retinal ganglion cells (hRGCs) were seeded at a density of 30,000–40,000 cells per Matrigel-coated coverslip (with 1.5 thickness) and cultured for 3 days. Following treatment with WAY-100635 at defined time points, culture media was removed, and cells were washed with 1× PBS. Cells were fixed with 4% paraformaldehyde for 15 min at 37 °C and subsequently permeabilized with 0.5% Triton X-100 in PBS for 5 min. Coverslips were then washed three times for 5 min each with washing buffer (1% donkey serum and 0.05% Triton X-100 in PBS). Cells were blocked in blocking buffer (5% donkey serum and 0.2% Triton X-100 in PBS) for 1 h at room temperature. Primary antibodies against Tom20 (Santa Cruz), cAMP (Bio-Techne), 5-HT1A (Abcam), and PGC1α (Abcam) were diluted 1:200 in blocking buffer and applied to coverslips, followed by overnight incubation at 4 °C. The next day, cells were washed three times with washing buffer and incubated for 2 h at room temperature in the dark with species-specific, fluorophore-conjugated secondary antibodies (1:500 dilution). DAPI (1.43 µM) was added during the second wash to label nuclei. Following final washes, coverslips were mounted onto glass slides using DAKO mounting medium. Fluorescence images were captured using a Zeiss LSM700 confocal microscope equipped with a 63×/1.4 NA oil immersion objective (Figs. 1f, j, 2a, e, h, j and 3a, and Supplementary Figs. 2a, 4a) and 40×/1.3 NA oil immersion objective (Fig. 1h and Supplementary 1a). Image analysis and quantification were performed using ImageJ software.

Western blot

Purified hRGCs were seeded at a density of 500,000 cells per well in Matrigel-coated 24-well plates and maintained in culture for 3 days. Cells were then treated with WAY-100635 at indicated time points, with media serving as the untreated control (UTC), as WAY was dissolved in dH_2O. Following treatment, cells were lysed in 100 µL of M-PER extraction buffer supplemented with 5 mM EDTA and protease inhibitors. Protein concentration was determined using the DC Protein Assay Kit II (Bio-Rad) with bovine serum albumin (BSA) as the standard, and absorbance was read using a microplate reader. Samples were prepared by mixing protein lysates (10–20 µg) with 1× Laemmli sample buffer and denaturing at 95 °C for 5 min. Proteins were separated on Mini-PROTEAN TGX precast gels (Bio-Rad) using Tris-Glycine-SDS running buffer at 100 V until the dye front reached the bottom of the gel. Proteins were transferred onto PVDF membranes pre-activated with methanol using Tris-Glycine transfer buffer containing 20% methanol, at 30 V for 2 h at 4 °C. Membranes were blocked with 5% non-fat dry milk in TBST (Tris-buffered saline with 0.5% Tween-20) for 2 h at room temperature and then incubated overnight at 4 °C with primary antibodies against Tom70 (Santa Cruz), PGC-1α (Abcam), 5-HT1A (Abcam), and GAPDH (CST), all diluted 1:1000. After washing three times with TBST, membranes were incubated with HRP-conjugated anti-rabbit secondary antibody (CST) diluted 1:10,000 in 5% milk/TBST for 2 h at room temperature. Following three additional TBST washes, signal was developed using Clarity Max Western ECL substrate (Bio-Rad) and visualized with a Bio-Rad ChemiDoc Gel Imager. Protein bands were quantified by measuring raw integrated density using ImageJ software. Each band was normalized to the corresponding GAPDH (or actin) loading control. Additionally, each treatment condition was normalized to its respective vehicle control. Quantification was based on expected molecular weights as per antibody datasheets and published references.

Antisense Oligonucleotide (ASO) design and treatment

Non-targeting scrambled control ASOs and PGC-1α-targeting ASOs were synthesized by Integrated DNA Technologies (IDT). All ASOs were modified with IDT's Affinity Plus chemistry. ASO sequences are listed in Supplementary Data 1. The PGC-1α-targeting ASOs were designed to bind the 3′ untranslated region (3′UTR) of the human PGC-1α mRNA and were applied to H7-hRGC^{WT}. ASOs (1 µM) were delivered via standard gymnotic uptake (without a transfection reagent). For knock-down analysis by western blots (Fig. 2g), cells were collected after indicated timepoints post-first ASO addition and ASOs were replenished every 48 h for the duration of the experiment. For mitochondrial mass measurements by confocal immunofluorescence (Fig. 2h–k), cells were treated with ASOs (1 µM) for 24 h, then treated with WAY (5 µM) by exchanging media containing WAY and ASO for the indicated timepoints.

JC1 imaging

Purified hRGCs were seeded at a density of 40,000 cells per Matrigel-coated glass-bottom MatTek dish (No. 1.5 thickness) and cultured for 3 days. Cells were then treated with WAY-100635 at designated time points. Following treatment, cells were washed with iNS media and incubated with JC-1 dye (1:100 dilution in iNS; final volume 250 µl) for 30 min at 37 °C in a 5% CO_2 incubator. After incubation, the JC-1 media was removed, cells were washed with fresh iNS, and 2 ml of iNS was added before transferring the dish to a live-cell imaging chamber (Tokai Hit) maintained at 37 °C and 5% CO_2. Confocal z-stack images were acquired using a Zeiss LSM700 confocal microscope with a 63×/1.4 NA oil immersion objective. ImageJ was used to generate sum projections of the red (J-aggregates) and green (JC-1 monomers) channels for quantitative analysis. Background red fluorescence, contributed by tdTomato expression, was subtracted based on cytoplasmic intensity measurements. Green fluorescence background was measured from cell-free regions and similarly subtracted. Mitochondrial membrane potential was quantified by calculating the red-to-green fluorescence ratio, which was normalized to the corresponding untreated control or average DMSO-treated condition for each cell line.

Tetramethylrhodamine methyl ester (TMRM) imaging

Purified hRGCs were seeded at a density of 40,000 cells per Matrigel-coated glass-bottom MatTek dish (No. 1.5 thickness) and maintained in culture for 3 days. Cells were treated with WAY-100635 at designated time points. Prior to staining, cells were washed twice with 750 µL of iNS media and then incubated with 250 µL of iNS media containing TMRM (Thermo Fisher) at a final concentration of 100 nM for 30 min at 37 °C in a 5% CO_2 incubator. TMRM was freshly prepared from a 100 µM DMSO stock solution by 1:1000 dilution (1.5 µL in 1.5 ml iNS). After incubation, the dye was removed, and cells were washed twice with 750 µL of iNS. Finally, 1.5 ml of

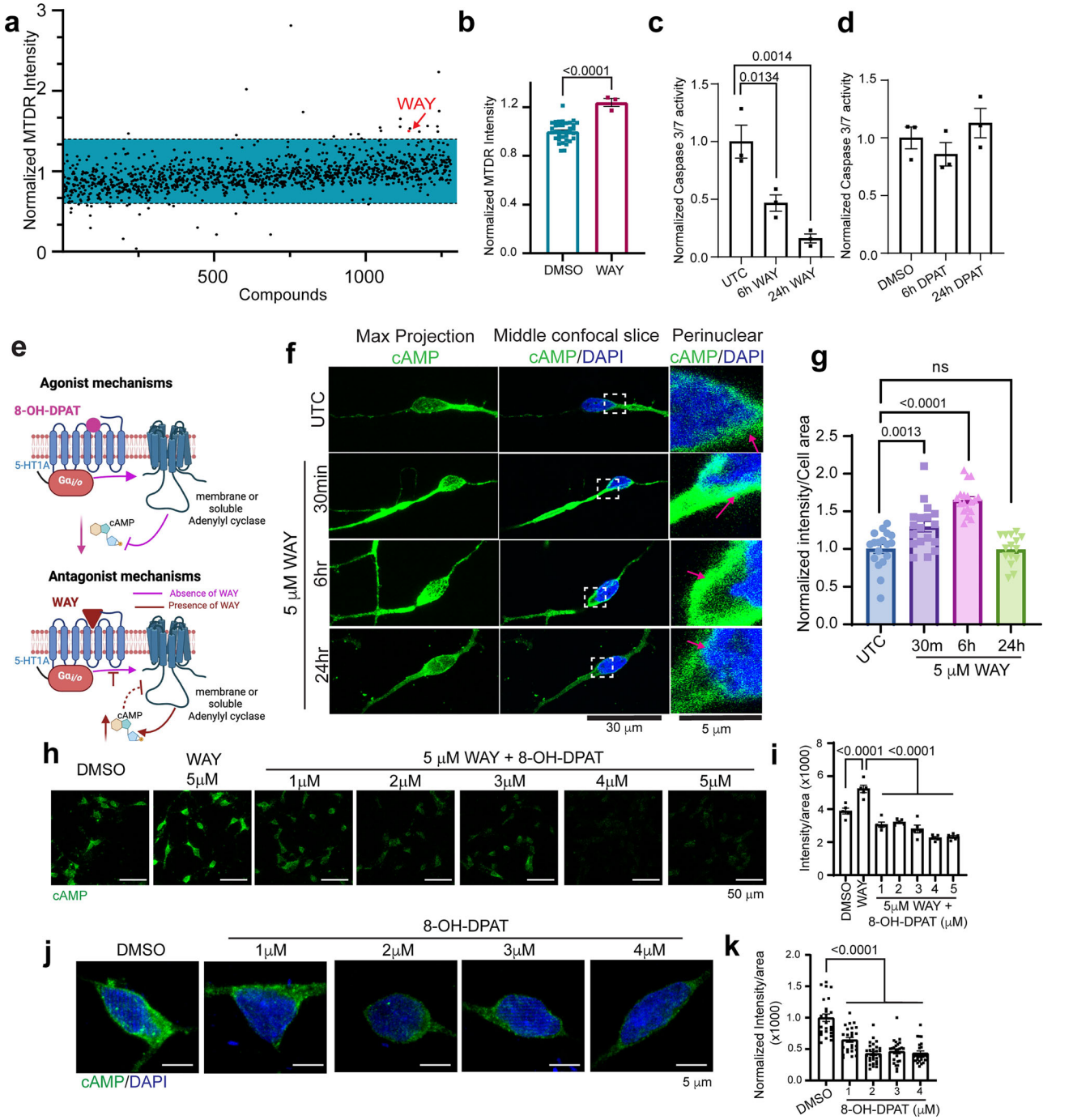

Fig. 1 | WAY-100635 engages 5-HT1A receptor to reversibly stimulate neuroprotective second messenger cAMP. a High-content screen of H7-hRGC^{WT} (derived from the H7-hESC reporter line) plotted for fold-change in MitoTracker Deep Red (MTDR) fluorescence; compounds altering mitochondrial mass by more than 40% lie outside the blue box, with WAY-100635 (WAY) highlighted in red. **b** Independent validation (5 μM, 24 h) confirms increased MTDR signal relative to DMSO vehicle control. Unpaired, two-tailed Student's *t* test; *n* (DMSO) = 36 and *n* (WAY) = 3 biological replicates; mean ± SEM. **c**, **d** Caspase-3/7 activity (Apo-ToxGlo-Triplex) after 24 h treatment with WAY (5 μM) or the 5-HT1A agonist 8-OH-DPAT (DPAT, 5 μM), normalized to untreated control (UTC). One-way ANOVA, Dunnett's post-hoc; *n* (UTC, 6 h and 24 h WAY/DPAT) = 3 culture wells. **e** Cartoon summarizing reciprocal cAMP signaling elicited by 5-HT1A antagonism (WAY) or agonism (DPAT). **f** Confocal immunofluorescence with anti-cAMP antibody (max projection and central z-plane) shows time-dependent perinuclear cAMP accumulation after WAY (red arrow). **g** Quantification of cAMP intensity per cell area from sum projections, normalized to UTC. One-way ANOVA, Dunnett's; *n* (UTC, 30 min, 6 h WAY) = 18 and *n* (24 h WAY) = 15 cells. **h**, **i** WAY pre-treatment (1 h, 5 μM) elevates cAMP, which is dose-dependently suppressed by subsequent DPAT (1–5 μM, 6 h). One-way ANOVA, Tukey's post-hoc; *n* (DMSO, WAY, WAY + 1 μM/2 μM/3 μM/4 μM/5 μM 8OHDPAT) = 5 images per condition, 80–150 cells per image. Each data point represents one image. **j**, **k** DPAT alone (6 h) lowers basal cAMP. One-way ANOVA, Dunnett's post-hoc; *n* (DMSO/3 μM/4 μM DPAT) = 25, *n* (1 μM DPAT) = 26, *n* (2 μM DPAT) = 28 cells. Quantification done from sum projections as in (**g**). Error bars represent SEM throughout. DMSO served as vehicle for DPAT. Statistical significance is indicated by exact *P* values shown between the compared groups in each panel.

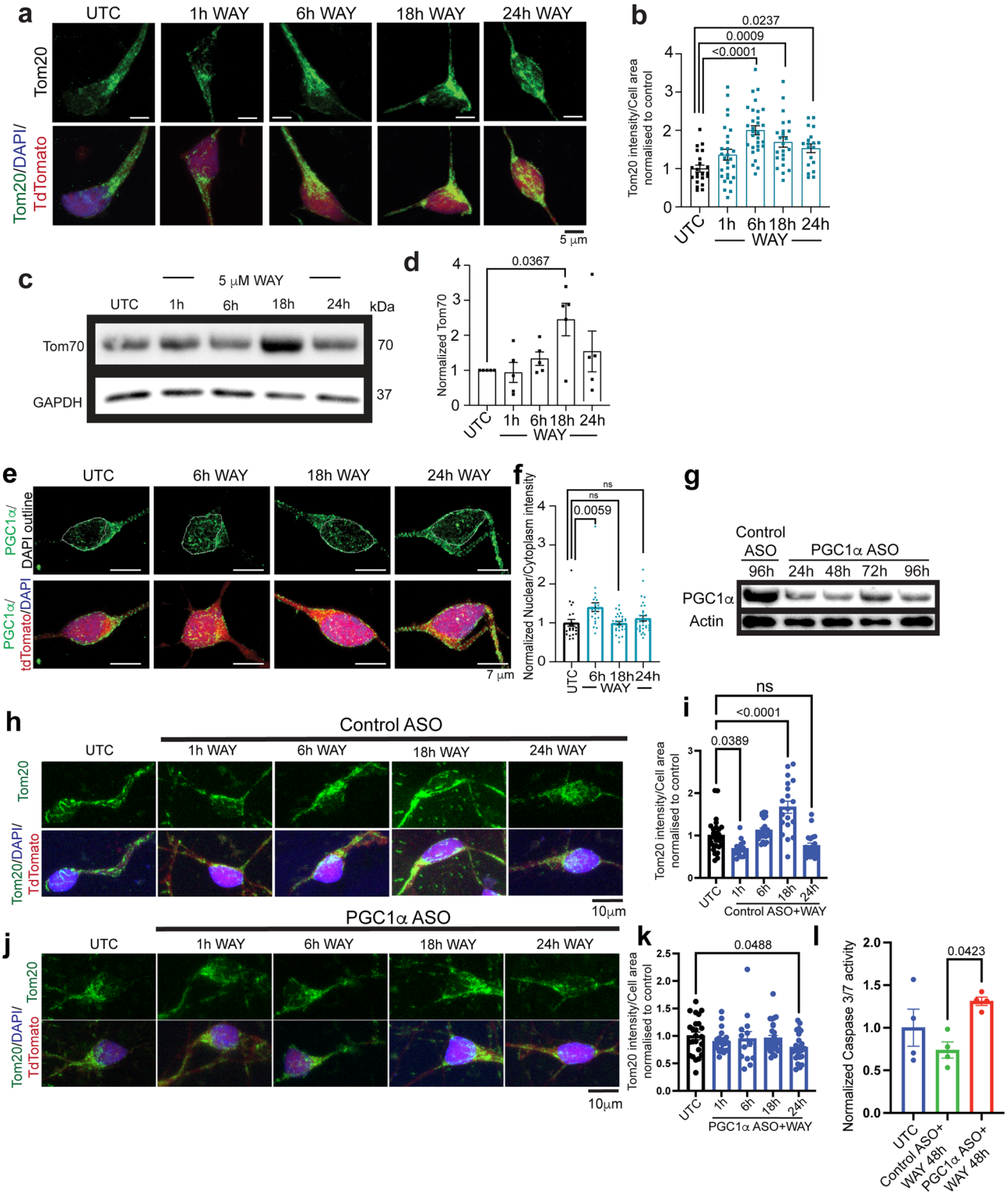

fresh iNS was added, and dishes were transferred to a live-cell imaging chamber (Tokai Hit) set at 37 °C and 5% CO_2. Confocal z-stack images were acquired using a Zeiss LSM700 confocal microscope equipped with a 63×/1.4 NA oil immersion objective. Image analysis was performed using ImageJ. Sum projections of TMRM fluorescence (red channel) were generated, and background fluorescence contributed by cytoplasmic tdTomato expression in hRGCs was subtracted. Fluorescence intensity was quantified by applying a threshold to define mitochondria-rich regions, and signal was normalized to cell area. All fluorescence measurements were normalized to the average signal of DMSO-treated controls for each experimental condition.

Multi-electrode array (MEA)

Stem cell-derived hRGCs were seeded at a density of 500,000 cells per well onto MEA plates (CytoView MEA 24-White, Axion Biosystems) and cultured for 11 days in iNS media, with media changes every other day. On day

Fig. 2 | WAY-100635 reversibly induces mitochondrial biogenesis in hRGCs via PGC-1α. a Representative confocal images (max projection of z-stacks) of H7-hRGC^{WT} expressing tdTomato (red), and stained for nucleus (DAPI, blue), mitochondria (Tom20, green) at the indicated times after 5 μM WAY. **b** Tom20 fluorescence per cell area (sum projection) expressed as normalized to untreated control (UTC). One-way ANOVA, Dunnett post-hoc; *n* (UTC) = 22, *n* (1 h WAY) = 28, *n* (6 h WAY) = 30, *n* (18 h WAY) = 23, and *n* (24 h WAY) = 19 cells; **c**, **d** Immunoblot and densitometry for Tom70 after WAY (5 μM) treatment. Values are Tom70/GAPDH, normalized to UTC. one-way ANOVA, Dunnett's post-hoc; *n* (UTC, 1 h, 6 h, 18 h and 24 h WAY) = 5. **e**, **f** Confocal images (max projection) and quantification of PGC-1α nuclear translocation following WAY (5 μM) treatment. Data are nuclear-to-cytoplasm intensity ratios from sum projections normalized to UTC; One-way ANOVA, Tukey's post-hoc; *n* (UTC) = 22, *n* (6 h WAY) = 23, *n* (18 h WAY) = 29, and *n* (24 h WAY) = 33 cells. **g** Time-course immunoblot validating knock-down of PGC-1α with a 3′-UTR-targeting antisense oligonucleotide (ASO) versus non-targeting control. **h**–**k** Confocal image (max projection) of H7-hRGC^{WT} stained for mitochondria (Tom20) after 24 h control or PGC-1α ASO pretreatment followed by WAY (5 μM, 1–24 h). **h**, **i** Control ASO permits the expected rise in mitochondrial mass; **j**, **k** PGC-1α ASO blocks it. Quantification of Tom20 intensity done per cell area from sum projections normalized to UTC. One-way ANOVA, Dunnett's post-hoc; *n* (UTC, for Control ASO) = 29, *n* (Control ASO + 1 h WAY) = 15, *n* (Control ASO + 6 h WAY) = 24, *n* (Control ASO + 18 h WAY) = 19, *n* (Control ASO + 24 h WAY) = 20, *n* (UTC, for PGC-1α ASO) = 24, *n* (PGC-1α ASO + 1 h WAY) = 23, *n* (PGC-1α ASO + 6 h WAY) = 13, *n* (PGC-1α ASO + 18 h WAY) = 29, and *n* (PGC-1α ASO + 24 h WAY) = 26 cells. **l** Caspase-3/7 activity (ApoToxGlo-Triplex) after 24 h ASO pretreatment +48 h WAY, plotted as normalized to UTC. One-way ANOVA, Tukey's; *n* (UTC, Control ASO + 48 h WAY and PGC-1α ASO + 48 h WAY) = 4. Error bars represent SEM. Statistical significance is indicated by exact *P* values shown between the compared groups in each panel.

11, the media was refreshed, and the plate was placed into the Maestro Edge MEA recording system (Axion Biosystems) equipped with environmental control to maintain 37 °C and 5% CO_2. Following a 15-min equilibration period, spontaneous neuronal activity was recorded for 3 min every 3 h over 24 h. After this baseline recording phase, WAY-100635 was added directly to the wells at a concentration of 5 μM, and gentle mixing was performed to ensure even distribution. Recordings were then continued every 3 h for another 24 h. Data analysis was performed by averaging the mean firing rate from all 16 electrodes per well for each time point. The nine pre-treatment recordings were averaged to determine the baseline activity, while the nine post-treatment recordings were averaged to quantify the effects of WAY treatment.

Seahorse analysis

Purified hRGCs were seeded onto Matrigel-coated Agilent Seahorse XF96 cell culture microplates at a density of 250,000 cells per well and cultured for 2 days prior to the assay. For hRGC differentiation culture day 2–6 treatment, cells were treated with 5 μM WAY along with the differentiation small molecules. Twenty-four hours before the assay, culture media were replaced with 100 μL iNS containing 5 μM WAY. The day before the assay, Seahorse XF sensor cartridge was hydrated with 200 μL sterile water per well and incubated overnight at 37 °C in a non-CO_2 incubator. On the day of assay, water was replaced with pre-warmed XF calibrant buffer (Agilent), and cartridge was incubated for an additional 45–60 min. Seahorse assay medium was prepared using XF DMEM supplemented with 21.25 mM glucose, 0.36 mM sodium pyruvate, and 1.25 mM L-glutamine, with the pH adjusted to 7.38–7.42 at 37 °C. For different assays, the following compounds were loaded into the cartridge ports: for the Mito Stress Test, 2 μM oligomycin, 2 μM FCCP (optimized from prior titration), and 0.25 μg/ml rotenone + 0.5 μM antimycin A; for the ATP rate assay, 2 μM oligomycin and 0.25 μg/ml rotenone + 0.5 μM antimycin A; and for the glycolytic rate assay, 0.25 μg/ml rotenone + 0.5 μM antimycin A and 17.5 mM 2-deoxy-D-glucose (2-DG). To prepare wells for the assay, 60 μL of iNS was removed from each well and replaced with 140 μL of Seahorse assay medium, followed by another media exchange step using 140 μl fresh assay medium to achieve a final volume of 180 μL per well. Empty wells were filled with 180 μL assay medium. For hRGCs, cell distribution and confluence were recorded using Incucyte S3 (Sartorius) via brightfield and tdTomato fluorescence imaging for normalization. The plate was then incubated at 37 °C in a non-CO_2 incubator for 45 minutes prior to assay. After calibration of the sensor cartridge in the Seahorse XFe96 Analyzer (Agilent) using WAVE software, the cell plate was loaded, and the selected assay was run. Post-assay, image analysis was performed using ImageJ to measure cell area for normalization in hRGCs, while day 2–6 WAY treated or untreated differentiation culture data were normalized using flow cytometry-based cell counts. Data were processed and exported using Seahorse Wave Desktop software and associated Excel macros (Agilent).

Measurement of hRGC differentiation efficiency

To evaluate hRGC differentiation efficiency, entire wells containing mixed populations of differentiating cells were dissociated into single-cell suspensions using Accutase. Cells were incubated with Accutase for 10–15 min at 37 °C, followed by gentle trituration in iNS media to achieve a homogeneous single-cell suspension. The cells were centrifuged and resuspended in fresh iNS media. Single-cell suspensions were analyzed on the Attune NxT flow cytometer (Thermo Fisher). Live cells were first identified using forward and side scatter properties, and doublets were excluded by gating on the singlet population using FSC-A vs. FSC-H plots (Supplementary Fig. S7 for gating). The percentage of tdTomato positive hRGCs was then assessed within the singlet population.

qPCR

hESCs were seeded at a density of 15,000 cells per well in Matrigel-coated 24-well plates and maintained for 7 days. From day 2 to day 6, cells were treated daily with 5 μM WAY-100635, alongside the standard differentiation small molecules. On day 7, the media were aspirated, and cells were incubated with 200 μL Accutase for 10 minutes at 37 °C. The enzymatic reaction was quenched with 400 μL of iNS medium, followed by centrifugation at 150 × *g* for 6 min. Supernatants were removed, and cell pellets were stored at −20 °C until further processing. Total RNA was extracted using the RNeasy Mini Kit (Qiagen, #74104) according to the manufacturer's protocol. RNA concentration was quantified using a NanoDrop 2000c spectrophotometer (Thermo Scientific), and 6 μL (1 μg) of RNA was used for cDNA synthesis using the Applied Biological Materials cDNA Synthesis Kit (#G492). Quantitative PCR (qPCR) was performed using BlasTaq™ qPCR MasterMix in a 20 μL reaction containing 100 ng of total cDNA per well, on a QuantStudio 6 Flex Real-Time PCR system (Applied Biosystems). Primers used for gene expression analysis are listed in Supplementary Data 1. GAPDH was used as a housekeeping gene for normalization. ΔCt values were calculated relative to the housekeeping gene, and ΔΔCt values were determined relative to the mean ΔCt of control (untreated) samples. Each condition was measured in triplicate (technical replicates), with 3–4 independent biological replicates.

Cell cycle stage assessment

Cell cycle distribution was assessed by measuring DNA content using propidium iodide (PI) staining, following an established protocol[23]. Cells were dissociated using Accutase, pelleted, and fixed overnight at −20 °C in 70% ice-cold ethanol. Following fixation, cells were washed twice with ice-cold PBS and resuspended in PBS containing 20 μg/ml PI, 0.1% Triton X-100, and 100 μg/ml RNase A. The suspension was incubated at room temperature for at least 30 min to allow sufficient DNA staining. Flow

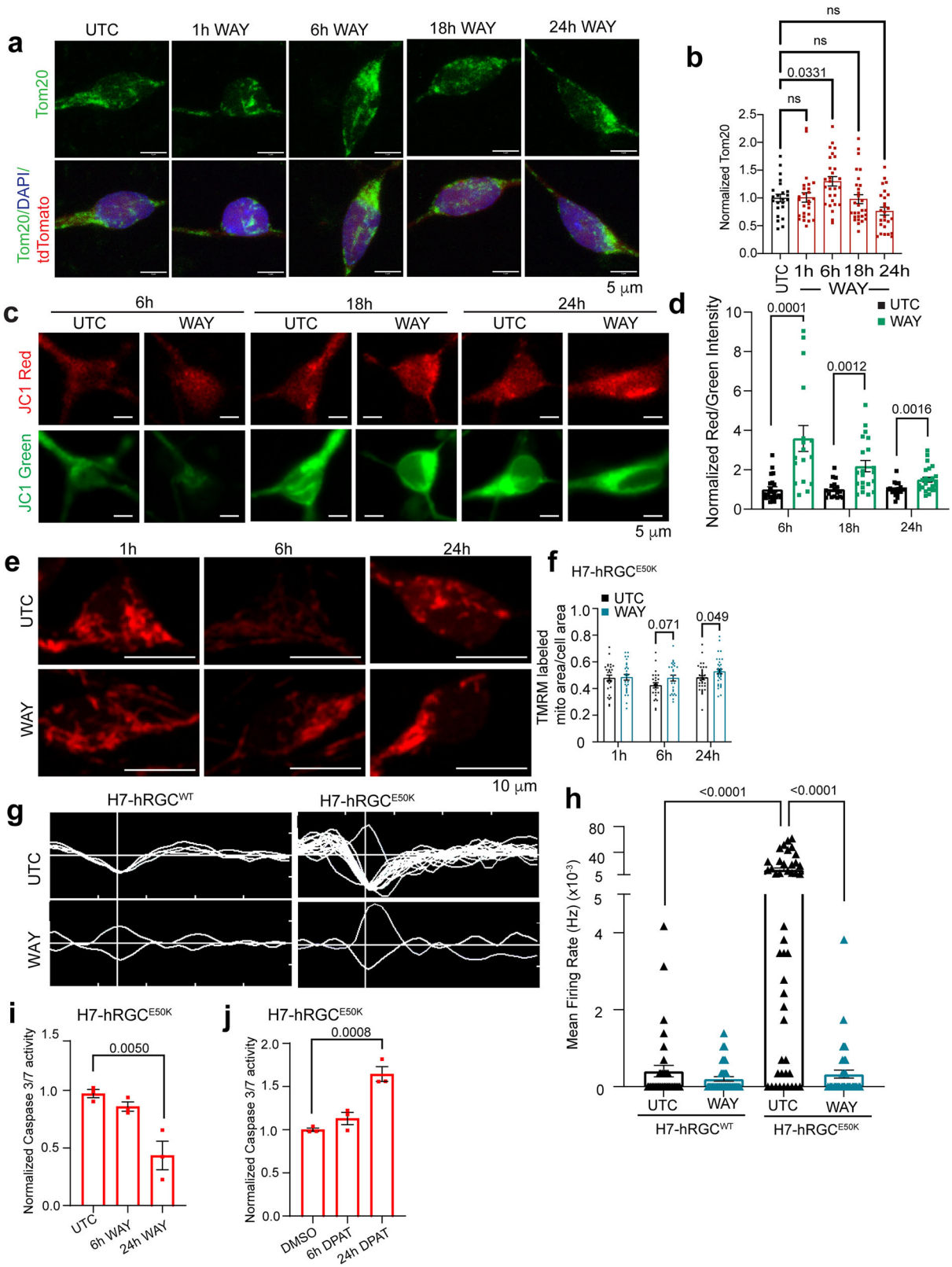

cytometric analysis was performed using the Attune NxT flow cytometer (Thermo Fisher). Doublets were excluded by gating on the singlet population (FSC-A vs. FSC-H), and PI fluorescence was measured to quantify DNA content. Data were analyzed using ModFit LT software (Verity Software House), which modeled the PI fluorescence distribution to determine the proportion of cells in G0/G1, S, and G2/M phases based on DNA content. Results were visualized as histograms showing phase-specific peaks with corresponding percentage values.

Electron microscopy

Human ESCs (hESCs) were seeded at a density of ~350,000 cells per well in 6-well Matrigel-coated plates and maintained for 7 days. From day 2 to day

Fig. 3 | WAY-100635 transiently induces mitochondrial biogenesis to restore homeostasis and provide protection to glaucomatous OPTN^{E50K} hRGCs. **a** Representative confocal images (max projection of z-stacks) of H7-hRGC^{E50K} expressing tdTomato (red), and stained for nucleus (DAPI, blue), mitochondria (Tom20, green) at the indicated times after 5 μM WAY treatment. **b** Tom20 fluorescence per cell area from sum projections, expressed normalized to untreated control (UTC). One-way ANOVA, Dunnett's post-hoc; *n* (UTC) = 23, *n* (1 h WAY) = 26, *n* (6 h WAY) = 28, *n* (18 h WAY) = 29, and *n* (24 h WAY) = 26 cells. **c** Mitochondrial membrane potential assessed with JC-1 live-cell images, **d** and red/green fluorescence ratios normalized to corresponding untreated control (UTC) ratios show a significant increase after WAY treatment. Unpaired, two-tailed Student's *t* test; *n* (6 h UTC) = 22, *n* (6 h WAY) = 17, *n* (18 h UTC) = 17, *n* (18 h WAY) = 21, *n* (24 h UTC) = 22, and *n* (24 h WAY) = 24 cells. **e**, **f** Mitochondrial membrane potential measurements with TMRM labeling: **e** representative live cell images, **f** and quantified TMRM labeled mitochondria area per cell area from sum projections. Unpaired, two-tailed Student's *t* test; *n* (1 h UTC) = 27, *n* (1 h WAY) = 28, *n* (6 h UTC) = 26, *n* (6 h WAY) = 26, *n* (24 h UTC) = 35, and *n* (24 h WAY) = 35 cells. **g** Representative action potential firing spikes from a single microelectrode array (MEA) sensor over 3 min under the indicated conditions. **h** Mean firing rate (16 sensors/well) pooled across wells. Two-way ANOVA, Tukey's post-hoc; *n* (H7-hRGC^{WT} UTC/WAY) = 4, and (H7-hRGC^{E50K} UTC/WAY) = 5 wells. Each data point is from a single recording, while multiple recordings were acquired over 24 h for each well. **i**, **j** Caspase-3/7 activity (ApoToxGlo-Triplex) after treatment with WAY (5 μM) or DPAT (5 μM), at specific time points, normalized to UTC or DMSO, respectively. One-way ANOVA, Dunnett's post-hoc; *n* (UTC, 6 h WAY, 24 h WAY, DMSO, 6 h DPAT, 24 h DPAT) = 3 culture wells. Error bars are SEM. Statistical significance is indicated by exact *P* values shown between the compared groups in each panel.

6, cells were treated with 5 μM WAY-100635 along with the standard differentiation small molecules. In another 6-well plate, hESCs were seeded following routine passaging procedures using Gentle Cell Dissociation Reagent when cultures reached 70–80% confluency. These cells were maintained until they reached 80–90% confluency and were then used as pure stem cell samples for EM without any differentiation. On day 7, media were aspirated and ~1 million cells per condition were collected and pelleted by centrifugation at 1000 × *g* for 10 min at 4 °C. Cell pellets were fixed overnight at 4 °C in 1 mL of 0.1 M cacodylate buffer (pH 7.4) containing 2.5% glutaraldehyde and 2% paraformaldehyde (Electron Microscopy Sciences, Hatfield, PA, USA). Pellets were washed three times with 4 mL of 0.1 M cacodylate buffer, then subjected to secondary fixation with 4 mL of 0.1 M cacodylate buffer containing 1% osmium tetroxide (OsO_4) and 1.5% potassium ferrocyanide for 1 h at room temperature. Samples were dehydrated through a graded ethanol series: 30% ethanol for 10 min, 50% for 30 min, 70% for 30 min, followed by two washes in 95% ethanol for 15 min each, and two washes in 100% ethanol for 30 min each. Infiltration was performed on a rotator at 60 rpm with 4 mL SPURR resin (Electron Microscopy Sciences) solutions mixed in increasing concentrations of resin-to-ethanol: 1:2 for 16 h, 1:1 for 24 h, 3:1 for 3 h, and 100% SPURR for 6 h. Pellets were embedded in BEEM capsules filled with 400 μL of fresh SPURR resin and polymerized by incubating at 70 °C for 12 h. Ultrathin sections (70 nm) were cut using a Leica ultramicrotome with a Diatome diamond knife and mounted on 200-mesh nickel grids. Grids were dried in a vacuum desiccator (SP Bel-Art, Wayne, NJ, USA) for 1 h before imaging. Electron micrographs were acquired using a Tecnai Spirit BioTwin transmission electron microscope (FEI, Hillsboro, OR, USA) operating at 80 kV, equipped with an AMT NanoSprint 6 CMOS camera (AMT, Woburn, MA, USA).

Animals

All animal experiments were approved by the Institutional Animal Care and Use Committee (IACUC) at the Indiana University School of Medicine and conducted in accordance with the ARVO Statement for the Use of Animals in Ophthalmic and Vision Research and the ARRIVE guidelines. Wild-type C57BL/6J male mice (2–3 months old) were obtained from The Jackson Laboratory (Bar Harbor, ME, USA) and housed under standard conditions at the Laboratory Animal Resource Center (LARC), Indiana University School of Medicine. In female mice, the estrous cycle-with its fluctuating levels of estrogen and progesterone, influences both neuronal injury and recovery processes. These hormonal variations modulate neuronal excitability, neurovascular dynamics, and the expression of neurotrophic factors[24,25]. Estrogen, in particular, plays a critical role in regulating mitochondrial function, thereby impacting cellular energy metabolism and neuronal resilience[26]. Given these influences, it is important to consider the stage of the estrous cycle when assessing outcomes in studies involving neuronal injury and regeneration. To avoid these complications, we have studied neuronal injury only in male mice. For the optic nerve crush (ONC) model, mice were divided into three groups (*n* = 3–6 per group): naïve, ONC, and WAY + ONC. All animals were acclimatized for one week prior to experiments. The WAY + ONC group received daily intraperitoneal injections of WAY-100635 (5 mg/kg body weight) for 5 days before ONC surgery. ONC was performed on day 0 in both the ONC and WAY + ONC groups, and WAY treatment was continued post-ONC for up to a day before sacrifice, depending on the experimental timeline. In an alternate cohort, post-treatment with WAY began 4 h after ONC and continued daily until a day before sacrifice. At the end of each experiment, animals were euthanized, and eyes, optic nerves, kidneys, and livers were collected. Body weight was recorded at 5 days prior to ONC, on the day of ONC, and at the time of sacrifice.

For the elevated intraocular pressure (IOP) model using microbead injection, mice were assigned to three groups: PBS injection (saline control), microbead-injected (MB), and microbead-injected plus WAY treatment (WAY + MB). All animals were acclimatized for one week. The WAY + MB group received daily intraperitoneal injections of WAY (5 mg/kg body weight) for 6 days prior to microbead injection, which was performed on day 0 in both the MB and WAY + MB groups. WAY treatment continued daily post-injection. At the end of the study, animals were euthanized, and eyes were harvested for further analysis.

In both the optic nerve crush model (Fig. 6) and the high-IOP glaucoma model (Fig. 7), experimental groups were compared against their respective controls (naïve and saline-treated, respectively). However, the primary objective of this study was to evaluate the therapeutic efficacy of WAY. Accordingly, all key analyses focused on comparing untreated versus WAY-treated groups to determine whether WAY confers structural, functional, and neuroprotective benefits across models of RGC injury. The experimental unit is a single animal. Approximately, a total of 70 animals were used in the study. Published studies commonly employ group sizes of *n* = 3–5 animals per group for both optic nerve crush and high-IOP glaucoma models[27–30]. We did not pre-specify or compute effect sizes with confidence intervals for this study. A priori sample sizes were based on published literature in these models, which we have followed here for quantitative assessments. All animals assigned to each experimental group were included in the analysis unless they died unexpectedly during the experiment period, in which case they were excluded from further evaluation. Animals were initially randomized into housing cages by LARC staff. These cages were then randomly assigned to the different experimental groups. To minimize potential confounders related to treatment order and measurement sequence, all the procedures were randomly assigned across groups on each experimental day. In addition, cage positions within the animal room were reorganized every three days to reduce location-dependent environmental bias. Animal vision test and MRI experiments were done in a double-blinded manner, in which cage identity was masked and coded by one personnel and data acquired by other personnel without knowing the cage identity. All mice are acclimatized for at least 7 days before the start of any experiment. Animal experiments are done in the IU School of Medicine Laboratory Animal Resource Center (LARC) approved facilities. Animals are maintained and housed in regular condition by the LARC-approved personnel. No special housing was used. We did not observe any unexpected adverse events during animal care and monitoring. We closely

monitored the animals for signs of distress, such as body weight loss, and behavior as humane endpoints. No animals were sacrificed due to adverse effects.

Optic nerve crush mouse model

Mice were anesthetized using 1.5–2% isoflurane (Akorn, Illinois, USA), and 0.5% proparacaine hydrochloride ophthalmic drops (Bausch + Lomb, Laval, Canada) were administered to both eyes for local anesthesia. Phenylephrine Hydrochloride ophthalmic Solution (Akorn, Illinois, USA) was also administered to dilate the pupils. A small incision was made in the upper conjunctiva, and the eyeball was gently retracted outward using fine forceps. A second pair of forceps was used to carefully open the connective tissue surrounding the optic nerve. Under a dissecting microscope, the optic nerve was located and crushed ~1 mm behind the globe using calibrated forceps for a duration of 5 s. Following the optic nerve crush (ONC), the eye was gently repositioned into the orbit, and the mouse's head was released. To prevent infection and ensure eye lubrication during recovery, erythromycin ophthalmic ointment USP, 0.5% (Bausch + Lomb, Laval, Canada) was applied. Animals were monitored continuously until full recovery from anesthesia was confirmed.

Bead-injected high IOP mouse model

Mice were anesthetized with 1.5–2% isoflurane, and 0.5% proparacaine hydrochloride eye drops were applied for topical anesthesia. Phenylephrine Hydrochloride ophthalmic Solution was also administered to dilate the pupils. Under general anesthesia, microbeads were injected unilaterally into the anterior chamber of the mouse eye following established methods[31,32]. Briefly, <50 μm glass cannulas connected to a Hamilton syringe were used for injection. Microbeads were sterilized by placing them in 100% ethanol in 0.5 mL Eppendorf tubes, followed by centrifugation, resuspension in ethanol, and repeating this wash step twice. They were then washed and resuspended in sterile phosphate-buffered saline (PBS), and the final bead pellet was aspirated directly into a glass micropipette. For injection, a glass cannula was loaded sequentially first with 1 μL viscoelastic solution Healon (10 mg/mL sodium hyaluronate, Johnson & Johnson) then 2 μL of 1 μm and 2 μL of 6 μm polystyrene beads, which ensured maximum retention of the beads after cannula withdrawal. The left eye was gently proptosed and the cannula was inserted into the inferior region of the anterior chamber. The bead solution was slowly injected over a 45-second period, and the cannula was left in place for 2 min post-injection to minimize efflux. Mice were monitored carefully post-procedure until they fully regained consciousness.

Intraocular pressure measurement

Intraocular pressure (IOP) was measured under anesthesia (1.5–2% isoflurane) using the TonoLab rebound tonometer (TioLat, Inc., Helsinki, Finland). For each eye, five consecutive measurements with optimal quality grading were recorded and averaged to obtain a final IOP value. Baseline IOP was measured prior to microbead injection, and subsequent measurements were taken at designated time points following the injection to monitor changes in IOP over time.

Cumulative intraocular pressure (IOP) analysis

Cumulative IOP exposure was quantified using the Area Under the Curve (AUC) function in GraphPad Prism. IOP values are collected at identical time points were plotted against time, and AUC was computed using the trapezoidal method. Because all groups were measured at the same time intervals, AUC provided a valid metric of overall IOP burden. Biological replicates at each time point were averaged before AUC calculation by Prism, and incorporated variance to generate standard errors. Since Prism does not directly compare AUCs, the resulting AUC and SEM values were transferred into a Grouped table (mean, SEM, *n*), with degrees of freedom (df) for each group defined as the number of IOP measurements for all the time points minus the number of time points; *n* was set to df +1 to allow correct statistical testing. Group differences in cumulative IOP were evaluated using one-way ANOVA with appropriate post-hoc correction. For details, please see Prism's analysis methods (https://www.graphpad.com/support/faqid/2031/).

Retinal flat mounting and RGC count

Retinal tissues were collected and immersed in ice-cold PBS before being fixed in 4% paraformaldehyde. Fixed tissues were then incubated five overnights with either guinea pig or rabbit anti-RBPMS antibody (catalogue no. 1832-RBPMS or 1830-RBPMS, PhosphoSolutions, Aurora, CO) at a dilution of 1:200. To detect the primary antibody, an Alexa Fluor 647-labeled goat anti-guinea pig secondary antibody (catalogue no. A21450, Invitrogen, Carlsbad, CA) or Donkey anti-rabbit Alexa Fluor 647 (catalogue no. A31573, Invitrogen, Carlsbad, CA) was used. Nuclei were counterstained with DAPI during the final wash step. Eye cups were cut in a flower-petal shape and flat-mounted on slides using 0.45 μm black mixed cellulose ester (MCE) membrane filters. Coverslips were applied using Aqua-Poly/Mount mounting medium. Confocal immunofluorescence imaging was performed with a Zeiss LSM700 microscope using a 40×/1.3 NA oil objective. For each retina, eight z-stacked images were acquired from four quadrants, sampling both central and peripheral regions. Manual quantification of RBPMS-positive RGCs was performed on maximum intensity projections of the images.

Optic nerve cryosection preparation and staining

Cryosections are prepared following published methods[33] but with modifications. Optic nerves were fixed in 4% paraformaldehyde prepared in 0.1 M phosphate buffer (PB; NaH_2PO_4 and Na_2HPO_4 in Milli-Q water, pH 7.4) for 6 h at room temperature (RT). Following fixation, tissues were transferred to a 5% sucrose solution in phosphate buffer for 30 min, then sequentially incubated in increasing concentrations of sucrose (10%, 15%, and 20%) in 0.1 M PBS. For cryopreservation, tissues were incubated overnight at 4 °C in a mixture of 20% sucrose and OCT compound (Sakura Finetek) at a 2:1 ratio. The next day, tissues were oriented in Tissue-Tek cryo molds (Sakura Finetek) and snap-frozen in isopentane cooled with liquid nitrogen. Frozen tissues were sectioned using a Leica CM1850 cryostat (Leica Microsystems) at a thickness of 14 μm and mounted on Super Frost Plus microscope slides. After drying, the slides were stored at −80 °C until use. Prior to staining, slides were warmed a 37 °C incubator and tissue sections were outlined with an ImmEdge hydrophobic barrier pen (Vector Laboratories).

For staining, sections were first washed in Tris-buffered saline (TBS, pH 7.4) for 5 minutes, followed by pre-incubation in 100% methanol for 10 min. Blocking was performed using a solution of 10% donkey serum in TBS. Sections were then incubated overnight at 4 °C with a primary antibody against growth-associated protein 43 (GAP43) (1:1000; shared by Dr. Benowitz lab)[34–36], diluted in solution A (TBS2T: 300 mM NaCl, 0.1% Tween 20, pH 7.4) containing 2% BSA and 10% donkey serum. The following day, sections were rinsed in TBS2T for 1 h at 4 °C, followed by a 1-h rinse in solution A at room temperature, and then a final rinse in TBS2T for 1 h at room temperature. Sections were subsequently incubated for 2 h at room temperature with an AlexaFluor-488-conjugated donkey anti-sheep IgG secondary antibody (1:500; Thermo Fisher Scientific, #A11015), followed by washes in TBS2T (2 ×5 min) and TBS (5 min) at room temperature. Sections were mounted using one drop of DAKO mounting medium, coverslip, sealed with nail polish (Electron Microscopy Sciences), and allowed to dry overnight at room temperature before imaging. Confocal stitched immunofluorescence images were taken using Zeiss LSM700 microscope or Nikon AX R confocal microscopes. For quantification, GAP43-positive axons crossing a virtual line located at 0.5 mm distal to the optic nerve crush site were counted. Four sections per nerve, spaced at least 28 μm apart, were analyzed. The maximum section width was used to estimate the cross-sectional area at 0.5 mm, and this, along with section thickness and axon counts, was used to estimate the total number of axons at that distance, following the published method by Benowitz lab[37].

Retinal cross-sections and immunostaining

Mice were euthanized by CO_2 inhalation followed by cervical dislocation. Eyes were enucleated and briefly rinsed with PBS. Two small punctures were made at the junction of the cornea and sclera using a needle, and the eyes were fixed in 4% paraformaldehyde (PFA) in PBS for 15 min. The cornea was removed, followed by extraction of the lens and vitreous body. Retina was isolated. The retina was further fixed in 4% PFA for 60 min at room temperature. After fixation, eyecups were washed three times in PBS (5 min each) and cryoprotected by immersion in a graded sucrose series in PBS (5%, 10%, 15%, and 20% for 30 min each at room temperature), followed by overnight incubation at 4 °C in a 2:1 mixture of sucrose-PBS (20%) and OCT compound. The next day, the tissues were embedded in OCT (Tissue-Tek) and snap-frozen in liquid nitrogen vapor. Eyecups were cryosectioned at 10 µm thickness using a Leica CM3050S cryostat and stored at −80 °C until use.

For immunohistochemistry, cryosections were thawed and air-dried at 37 °C for 40 min. Sections were washed three times with 0.1% PBST (PBS + 0.1% Triton X-100), then blocked in PBST containing 5% goat serum for 16–24 h at 4 °C. Following blocking, sections were rinsed once and washed three times (5 min each) with PBST, then incubated overnight at 4 °C with primary antibodies diluted in PBST. The next day, sections were again rinsed once and washed three times with PBST before incubation with secondary antibodies and DAPI in PBST for 1 h at 4 °C. After final washes (three times for 5 minutes each), sections were mounted using DAKO mounting medium and coverslips. Confocal immunofluorescence imaging was performed with a Zeiss LSM700 microscope using a 40×/1.3 NA oil objective.

Photopic negative response (PhNR) recording by flash electroretinogram (ERG)

RGC function was assessed using the Celeris system (Diagnosys, Inc., Lowell, MA) in conjunction with Espion software (Diagnosys, Inc.). Electroretinograms (ERGs) were recorded 12 days following optic nerve crush (ONC). Mice were dark-adapted overnight, and all procedures were performed under dim red light (660 nm). Animals were anesthetized with isoflurane and positioned on a heated platform maintained at 37 °C. Pupils were dilated using 1% tropicamide (Somerset Therapeutics, FL), and topical anesthesia was applied using 0.5% proparacaine hydrochloride (Bausch + Lomb, NJ). Corneal hydration was maintained using Systane (Alcon, TX). A contact lens-type probe with an integrated electrode and stimulator, featuring a pinhole aperture, was placed on the cornea and aligned with the center of the pupil. The reference electrode was placed on the contralateral eye. PhNR recordings were obtained using 100 consecutive white-light flashes (20.0 cd·s/m²) on a rod-saturating green background (40 cd·s/m²) to elicit RGC-specific responses. The raw signal was filtered with a 0.125–40 Hz bandpass filter to minimize oscillatory artifacts. For each animal, the probe was positioned at three different angles to ensure consistent recording, and the PhNR amplitudes were averaged. PhNR amplitude was defined as the voltage from the baseline to the trough immediately following the b-wave, and implicit time (time to trough) was also recorded. After the procedure, animals were placed back in their home cages on heating pads covered with drapes. Cages were positioned such that only half rested on the heating pad (low temperature setting), allowing the mice to self-regulate body heat. Once fully ambulatory (~10–15 min), animals were returned to the animal facility.

Flash visual evoked potential (fVEP)

Flash visual evoked potentials (fVEPs) were recorded with the Celeris system integrated with Espion software (Diagnosys, Lowell, MA), 9 days after unilateral microbead injection. Animals were dark-adapted overnight and handled under dim red light (660 nm), as in the PhNR protocol. Mice were anesthetized with ketamine/xylazine (90/10 mg/kg, i.p.) and positioned on a 37 °C heated platform; pupils were dilated with1% tropicamide (Somerset Therapeutics, FL), and the cornea topically anesthetized with 0.5% proparacaine hydrochloride (Bausch + Lomb, NJ). Corneal hydration was maintained with PBS throughout recording. A contact-lens electrode with integrated stimulator and pinhole aperture was centered over the pupil of the stimulated eye; the reference electrode was placed on the contralateral eye, subdermal platinum needles were inserted into the cheek and the occipital scalp over visual cortex, and the ground was positioned at the base of the tail. Each eye was stimulated and recorded separately using 50 white-light flashes (1 cd·s/m²). Signals were acquired in Espion; waveforms were analyzed for peak amplitudes, and the negative area under the curve (AUC) was calculated in GraphPad Prism and used for group comparisons.

Optokinetic response (OKR) test

Following unilateral microbead (MB) left eye injection in mice pretreated with WAY-100635 (5 mg/kg body weight) for 6 days, daily post-treatment with WAY was continued for designated durations, and optokinetic response (OKR) testing was performed on Days 7 and 30 post-MB injections using mouse OptoMotry system (Cerebral Mechanics, Inc). The OKR test was used to assess visual function, specifically visual acuity (VA) and contrast sensitivity (CS). Mice were placed on a platform surrounded by four computer screens displaying moving sinusoidal gratings (12°/s) in either clockwise or counterclockwise directions. For VA testing, the gratings were presented at increasing spatial frequencies while maintaining fixed speed and contrast. Head-tracking movements in response to the gratings were recorded, with higher frequencies indicating better visual acuity. For CS testing, gratings were presented at a fixed spatial frequency and speed, but with decreasing contrast. CS was quantified as the lowest contrast eliciting a tracking response, reported as Michelson contrast: (max − min)/(max + min), where "max" and "min" represent the maximum and minimum contrast levels to which the mouse responded[38,39]. VA and CS values were recorded separately for clockwise and counterclockwise stimulus directions, as well as combined to obtain an averaged measure of visual performance.

Histology

The kidney and liver tissues from the naïve and WAY-treated mice were collected and fixed in 10% formaldehyde and processed for paraffin sectioning. Paraffin-embedded sections were stained with hematoxylin and eosin to study the histological changes under a light microscope.

Mass spectroscopic analysis

To evaluate whether WAY-100635 crosses the blood-retinal barrier, C57BL/6J mice were intraperitoneally injected with WAY-100635 (100 µL in PBS) at a dose of 30 mg/kg body weight. Mice were sacrificed at 4- and 24-h post-injection, and both blood and eye tissues were collected for analysis. For plasma collection, 75 µL of blood was drawn into heparinized micro-capillary tubes and centrifuged at 5000 rpm for 5 min. The separated plasma was transferred to fresh tubes and stored at −80 °C. For retinal analysis, the eyes were enucleated, and the retinas were rapidly dissected, flash frozen in liquid nitrogen, and stored at −80 °C until further use. Quantification of WAY-100635 in both plasma and retinal tissues was performed using mass spectrometry.

High-resolution diffusion MRI and tractography of mouse brains

High-resolution in vivo MRI was performed using a 9.4 Tesla Bruker 94/30 system (Billerica, MA, USA) with a 30 cm bore and a maximum gradient strength of 660 mT/m on each axis. Diffusion-weighted images (DWI) were acquired using a multi-shot 2D echo-planar imaging (EPI) sequence with the following parameters: matrix size = 100 ×86, field of view = 15 × 12.9 mm², in-plane resolution = 150 µm, slice thickness = 0.3 mm, echo time (TE) = 27 ms, repetition time (TR) = 3500 ms, and b-values of 600, 1200, 1800, and 3000 s/mm², along with four non-diffusion-weighted (b0) volumes. The acquired DWI data were denoised using the Marchenko–Pastur principal component analysis (MP-PCA) method[40], corrected for Gibbs artifacts via a local subvoxel shift algorithm[41], and

registered nonlinearly to structural T2-weighted images using symmetric normalization (SyN) to correct for EPI distortions, motion, and eddy currents[42]. Bias field correction was applied using the N4 algorithm implemented in ANTs[43]. Diffusion modeling included fitting the diffusion tensor imaging (DTI), diffusional Kurtosis Imaging (DKI), and neurite orientation dispersion and density imaging (NODDI) models to extract key diffusion metrics such as fractional anisotropy (FA), mean diffusivity (MD)[44], kurtosis fractional anisotropy (KFA), mean kurtosis (MK)[45], neurite density index (NDI), and orientation dispersion index (ODI)[46]. Brain masks were manually validated, and average B0 images were registered to a T2-weighted brain atlas using diffeomorphic registration. Atlas labels were then transformed back into subject space for anatomical reference. For tractography, tissue response functions were automatically derived from six target regions: optic tract (OT), lateral geniculate nucleus (LGN), and visual cortex (VC) bilaterally using MRtrix3. Fiber orientation distributions (FODs)[47] were computed via constrained spherical deconvolution, followed by probabilistic tractography (10 million streamlines, threshold 0.17)[47] and SIFT filtering to reduce reconstruction bias[48]. Key tracts between the optic tract, LGN, and visual cortex were extracted bilaterally to evaluate visual pathway connectivity.

Mouse RGC purification

Mouse eyes were dissected, and the retinae were isolated and enzymatically dissociated in 500 µL of 5 U/mL Dispase (stored at −20 °C) following mechanical trituration. After a 25-min incubation at 37 °C, the dissociated cells were blocked in HBSS containing 2% BSA, counted, and centrifuged at 150 × *g* for 6 min. If no pellet was visible, a second centrifugation at 800 × *g* for 6 min was performed. Cells were then incubated with anti-CD90.2 (Thy1.2) magnetic microbeads (3 µL beads in 90 µL MACS BSA per 10 million cells) for 30 min, washed, and subjected to magnetic-activated cell sorting (MACS) using sequential small columns prewashed with MACS BSA. After three washes per column and elution, the purified RGCs were collected by centrifugation. For Western blotting, the cell pellet was lysed in 100 µL of MPER buffer supplemented with EDTA and protease inhibitors. For flow cytometry, cells were centrifuged at 800 rpm for 7 min, resuspended in blocking buffer, fixed and permeabilized with chilled acetone (1:1), and incubated at −20 °C for 10 min. After washing and pelleting, cells were incubated with primary antibodies (1:100) Tuj1 for 25 min at room temperature, washed, and incubated with secondary Alexa Fluor 488 antibody, (1:1000) for 25 min. Labeled cells were washed, resuspended in PBS, and analyzed by flow cytometry.

Statistics and reproducibility

Samples treated with WAY-100635 or 8-OH-DPAT at different time points were considered independent biological replicates. For comparisons between two independent datasets, unpaired, two-tailed Student's *t* tests were performed; each data point represents an individual sample (Figs. 1b, 3d, f, 5d, g–j, q and 6k and Supplementary Figs. S2b, d, S5b). For comparisons involving three or more groups with a single independent variable, one-way ANOVA was used (Figs. 1c, g, i, k, 2b, d, f, i, k–l, 3b, i, j, 5c, 6b, c, 7c, f, q, and Supplementary Figs. S1b, S3c). When data involved two independent variables, two-way ANOVA was performed to assess main effects and interactions (Figs. 3h, 4b, c, e–g, 6e, i and 7h, i). Post-hoc comparisons were corrected using Dunnett's test when comparing to a control group, or Tukey's test when comparing among all groups. Graphs were generated using GraphPad Prism 10.0, and figures were assembled in Adobe Illustrator.

Reporting summary

Further information on research design is available in the Nature Portfolio Reporting Summary linked to this article.

Materials availability

This study did not generate new unique reagents.

Results

Identification of WAY-100635 that activates neuroprotective signaling in hRGCs through antagonizing 5-HT1A receptor

Building on our recent discovery that boosting mitochondrial biogenesis safeguards human stem-cell-derived hRGCs, including those carrying the glaucoma-linked OPTN^{E50K} mutation[20], we performed a high-throughput screen for druggable enhancers of mitochondrial health. We screened the LOPAC (Library of Pharmacologically Active Compound, Sigma) library in highly purified (>90%) hRGC cultures that recapitulate native RGC transcriptional and electrophysiological signatures, a method widely accepted in the field, and we routinely use[20–22]. Mitochondrial fitness was quantified by flow-cytometric measurement of MitoTracker Deep Red (MTDR) fluorescence, a sensitive readout of healthy membrane-potential-positive mitochondrial mass[49]. Compounds that elevated single-cell MTDR signal 40% above the median threshold were flagged as primary hits (Fig. 1a). Secondary triage required that a hit both (i) maintain an elevated MitoTracker Deep-Red signal and (ii) lower the apoptosis (cleaved-caspase-3 activity) in hRGCs. Only a few compounds met both benchmarks, and WAY-100635 maleate (WAY) delivered the most pronounced dual response (Fig. 1b, c). Coupled with its documented safety in human studies, these data positioned WAY as the lead candidate for downstream glaucoma-neuroprotection analyses. Notably, under culture conditions even wild-type (Wt) hRGCs suffer apoptosis over time[50]; WAY significantly reduced this baseline apoptosis, indicating a broad neuroprotective action independent of any obvious genetic defects, which is often the case for POAG. WAY is a well-characterized antagonist of the Gi/o-coupled 5-HT1A receptor. To test if the receptor agonist shows an opposite effect, we treated wild-type hRGCs with the bona fide 5-HT1A agonist 8-OH-DPAT (DPAT)[51,52]. However, DPAT did not affect cellular apoptosis (Fig. 1d), underscoring that the protective effect is linked to 5-HT1A antagonism by WAY. Together, these findings warrant WAY as a potent, mitochondria-restorative small molecule and establish 5-HT1A antagonism as a tractable axis for RGC neuroprotection.

RGCs endogenously release serotonin, a 5-HT1A agonist that engages Gi/o proteins, suppresses its cognate adenylyl-cyclase (AC) activity, and enforces low intracellular cyclic adenosine mono phosphate (cAMP) levels[53,54]. Accordingly, hRGCs exposed to serotonin, or the canonical agonist DPAT, this is expected to display diminished cAMP, whereas the antagonist WAY is predicted to competitively inhibit agonist binding leading to disinhibition of AC and cAMP elevation (Fig. 1e). Consistent with this model, WAY treatment elicited a rapid but fully reversible rise in cAMP that decayed to baseline with classical GPCR kinetics (Fig. 1f, g). Strikingly, the elevation was enriched in the perinuclear compartment (Fig. 1f), a spatial signature previously linked to neuroprotection[55,56]. Because these experiments were performed in highly purified hRGC cultures devoid of other cell types, the response is unequivocally cell-autonomous. Continuous exposure to WAY for six days produced repeated, non-desensitizing oscillations in cAMP (Supplementary Fig. S1), demonstrating that 5-HT1A antagonism can engage downstream signaling without driving irreversible, constitutive changes, an essential property for therapeutic use.

To confirm receptor specificity, we performed a competitive reaction to 5-HT1A by the agonist DPAT and antagonist WAY. Competitive binding studies in primate brain have established that both WAY-100635 (WAY) and DPAT engage 5-HT1A with high selectivity[57]. In hRGCs, WAY alone elevated cAMP, whereas DPAT alone lowered it, responses predicted for antagonism versus agonism at a Gi/o-coupled receptor (Fig. 1f, g, h–k). Co-application of DPAT completely abolished the WAY-induced cAMP rise (Fig. 1h, i), indicating direct competition at the same binding site. Although limited reports suggest off-target activity of WAY at DRD4 (Gi/o-coupled)[58,59] and DPAT at 5-HT7 (Gs-coupled)[60,61] as agonist, such interactions in hRGCs would have produced the opposite cAMP signatures, decrease for WAY and increase for DPAT, which we did not observe. These data demonstrate that WAY's neuroprotective action in hRGCs is mediated through 5-HT1A antagonism.

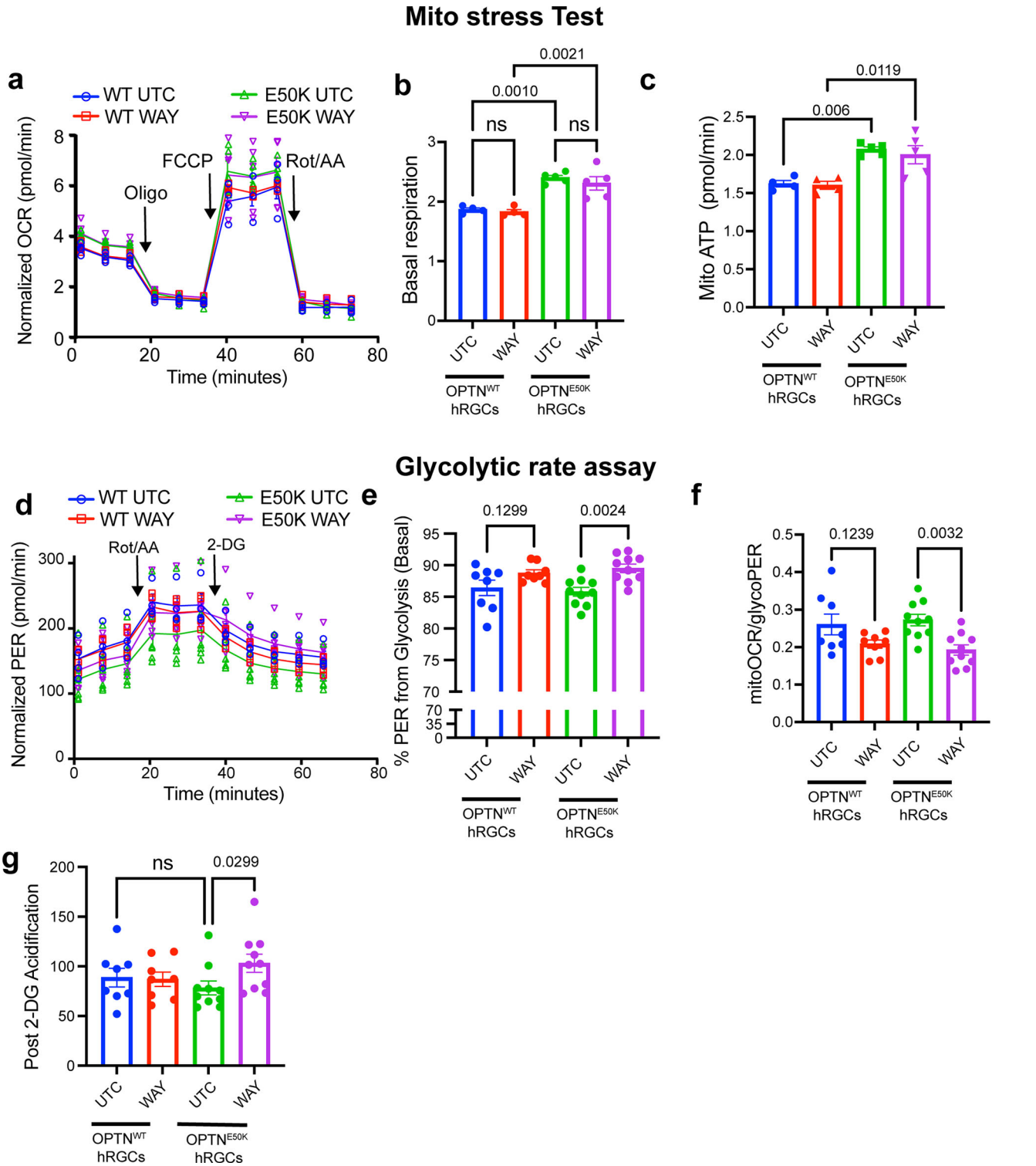

Fig. 4 | WAY-100635 induces glycolytic metabolic reprogramming in hRGCs. **a** Cell area normalized oxygen consumption rate (OCR) measured by Mito Stress Test in H7-hRGC^{WT} and H7-hRGC^{E50K} treated with or without WAY-100635 (5 μM) for 24 h. **b** Quantification of basal respiration, **c** and mitochondrial ATP production (pmol/min) in the WT and OPTN^{E50K} hRGCs. Two-way ANOVA with Tukey's; *n* (H7-hRGC^{WT} UTC/WAY) = 4, and *n* (H7-hRGC^{E50K} UTC/WAY) = 5 biological repeats. **d** Cell area normalized proton efflux rate (PER) from the Glycolytic Rate Assay in H7-hRGC^{WT} and H7-hRGC^{E50K} RGCs treated with or without WAY for 24 h, traces are averaged from *n* (H7-hRGC^{WT} UTC/WAY) = 4, and *n* (H7-hRGC^{E50K} UTC/WAY) = 6 biological repeats. **e** Quantification of basal percentage of PER from glycolysis, **f** mitoOCR/glycoPER ratio, and **g** post 2-DG acidification in respective hRGCs. Two-way ANOVA with Tukey's; *n* (H7-hRGC^{WT} UTC/WAY) = 8, and *n* (H7-hRGC^{E50K} UTC/WAY) = 10 biological repeats; Error bars are SEM. Statistical significance is indicated by exact *P* values shown between the compared groups in each panel.

WAY transiently induces mitochondrial biogenesis to restore homeostasis for hRGC protection

The increase in MTDR fluorescence observed after WAY exposure could reflect either enhanced mitochondrial biogenesis or a boost in membrane potential within the existing network. To distinguish these possibilities, we quantified mitochondrial mass during a WAY treatment time course by (i) confocal immunofluorescence using antibodies against the outer-membrane protein Tom20 and (ii) immunoblotting for Tom70. The imaging assay revealed a reversible surge in mitochondrial content that peaked at 6 h and returned to baseline by 24 h (Fig. 2a, b). The imaging peak coincided with maximal cAMP elevation, whereas the immunoblot assay showed a reversible surge, but the peak lagged by ~12 h (Fig. 2c, d), presumably due to the lag in protein turnover kinetics. Because nuclear PGC-1α orchestrates mitochondrial biogenesis and can be activated by cAMP[62], we examined its subcellular distribution. Confocal analyses showed a parallel, reversible enrichment of PGC-1α in nuclei (Fig. 2e, f), with kinetics that mirrored the 6-h biogenesis peak. Continuous replenishment of WAY for 6 days in the medium maintained this cyclic response for cAMP (Supplementary Fig. S1), indicating that the transient profile is intrinsic to the signaling cascade rather than drug depletion. To test whether PGC-1α is required for the mitochondrial biogenic pulse, we depleted PGC-1α with antisense oligonucleotides (ASOs) targeting the 3′ UTR (Fig. 2g). Control ASO-treated cells retained the characteristic rise-and-fall in mitochondrial mass after WAY (Fig. 2h, i). Strikingly, PGC-1α knockdown abolished this effect (Fig. 2j, k) and concomitantly blunted WAY-mediated protection against apoptosis (Fig. 2l). Collectively, these data demonstrate that WAY elicits a short-lived, cAMP-driven burst of mitochondrial biogenesis that is PGC-1α dependent and functionally linked to the compound's neuroprotective action in hRGCs.

WAY reversibly activated mitochondrial biogenesis in WT hRGCs. We therefore asked whether the same response occurs in NTG-associated OPTN^{E50K} hRGCs. Confocal immunofluorescence for the mitochondrial marker Tom20 revealed a transient rise in mitochondrial mass that peaked at 6 h, identical to the kinetics observed in WT cells (Fig. 3a, b). We previously have shown that OPTN^{E50K} hRGCs harbor fewer, but metabolically active overburdened mitochondria, stimulating biogenesis via targeting TBK1 relieves ATP demand from mitochondria and reduces apoptosis[20]. Consistent with this model, WAY increased mitochondrial membrane potential, measured with the potentiometric dyes JC-1 (red/green ratio) (Fig. 3c, d), and TMRM (mitochondrial area per cell area), across different treatment time points (Fig. 3e, f).

Mitochondrial depolarization drives excitotoxic hyperactivity[63]. Multi-electrode array recordings confirmed that OPTN^{E50K} hRGCs fire at higher spontaneous rates than WT controls, consistent with prior patch-clamp studies[64]; remarkably, WAY normalized firing frequency to WT levels (Fig. 3g, h). The observed mean firing rate of less than 1 Hz is typical of stem cell differentiated neurons as they possess sparse synaptic activity and lack astrocytic support that promotes neuronal activity[65–67]. Corroborating its neuroprotective effect, WAY reduced apoptosis in OPTN^{E50K} hRGCs, whereas the 5-HT1A agonist DPAT increased apoptosis (Fig. 3i, j). The OPTN gene is critical for mitochondrial homeostasis, and its E50K allele appears in ~17% of NTG patients with aggressive disease[19], highlighting its therapeutic relevance.

Together, these data show that antagonism of 5-HT1A by WAY transiently boosts mitochondrial biogenesis, restores mitochondrial health, suppresses excitotoxic activity, and ultimately protects OPTN^{E50K} hRGCs, highlighting a potential therapeutic avenue for normal-tension glaucoma.

WAY orchestrates cell-state specific metabolic reprogramming driving neuroprotective glycolysis in mature RGCs while enhancing oxidative phosphorylation in progenitor stem cells to accelerate differentiation

Under normal conditions, RGCs derive most of their ATP from mitochondrial oxidative phosphorylation (OXPHOS), however, excessive oxidative stress associated with OXPHOS promotes RGC degeneration[68]. Because WAY reversibly enhanced mitochondrial biogenesis and lowered apoptosis in both WT and OPTN^{E50K} hRGCs, we asked whether these benefits involve metabolic reprogramming. In the Seahorse Mito Stress Tests, that measures mitochondrial respiration, we observed higher oxygen consumption rate (OCR) for OPTN^{E50K} hRGCs for both control and WAY treatment under basal and FCCP induced maximum mitochondrial respiration (Fig. 4a). This led to the higher basal respiration (Fig. 4b), and mitochondrial ATP (MitoATP) synthesis for the OPTN^{E50K} hRGCs than WT cells but without having additional effects of WAY treatment (Fig. 4c). Increased mitochondrial ATP production for OPTN^{E50K} hRGCs is consistent to our earlier findings[20], but this is intriguing that even though WAY reversibly induces mitochondrial biogenesis and restores mitochondrial homeostasis it does not promote more mitochondrial respiration. This can be due to metabolic reprogramming in which WAY rebalances metabolic load between mitochondria and glycolysis to limit OXPHOS-related oxidative stress, yet meeting the ATP requirements for cellular physiology. To obtain direct evidence for change in glycolysis rate, we conducted Glycolytic-Rate Assay. Seahorse estimates glycolytic activity by measuring extracellular acidification rate (ECAR) and then separating the acidification due to glycolysis (lactate/H^+ export) from the acidification due to mitochondrial respiration (CO_2 hydration to $H^+ + HCO_3^-$). In the Glycolytic Rate assay, ECAR is corrected using OCR-derived mitochondrial CO_2 contribution, yielding a proton efflux-based readout that more specifically reflects glycolytic flux rather than total acidification alone. Inhibition of mitochondrial electron transport chain by Rot/AA inhibits proton source from mitochondria but drives maximum glycolytic capacity, hence corresponding proton efflux rate (PER) as compensatory ATP source. Next, the addition of 2-deoxy-D-glucose (2-DG) a glucose analog that inhibits glycolysis, drops PER confirms the proton efflux prior to 2-DG is from glycolysis (Fig. 4d). The fraction of PER attributable to glycolysis increased moderately in WT and significantly in the OPTN^{E50K} hRGCs under WAY treatment (Fig. 4d, e). Accordingly, the mitoOCR/glycoPER ratio declined moderately in WT and markedly in the OPTN^{E50K} hRGCs (Fig. 4f) reflecting glycolytic metabolic state. Following 2-DG application, residual acidification is not attributable to mitochondria but any residual glycolysis that are not inhibited. Post-2-DG acidification rose significantly in OPTN^{E50K} hRGCs treated with WAY without any effect on WT cells, implying higher basal glycolysis that is not completely inhibited (Fig. 4g). Collectively, these data show that WAY restores mitochondrial health yet paradoxically redirects cellular energetics toward aerobic glycolysis, avoiding further OXPHOS stimulation in the glaucoma-associated OPTN^{E50K} hRGCs. The pronounced shift toward aerobic glycolysis we uncover here mirrors protective metabolic adaptations reported across diverse neurodegenerative models including optic nerve injury[69,70].

Cues that drive pluripotent progenitors toward a neuronal fate can, in parallel, endow nascent neurons with heightened stress resistance[71]. Because stem cells maintain a low immature mitochondrial network, predominantly relying on glycolysis for ATP source[72], we asked whether stimulating mitochondrial biogenesis at this stage would enhance hRGC differentiation. We observed, hESCs treated with WAY-100635 (5 μM) displayed a robust increase in mitochondrial content, quantified by Tom20 immunofluorescence and Tom70 immunoblotting (Supplementary Fig. S2a–d). In contrast to the reversible rise observed in differentiated hRGCs, mitochondrial mass in hESCs progressively elevated during the 24-h time course, indicating a lineage-specific response to WAY. We next interrogated the developmental window during which WAY may enhance differentiation. The small molecule-based differentiation using RGC reporter stem cells used here produces tdTomato-positive hRGCs at around day 30 and reaches maximum number around day 45[22]. Cultures were pulsed with WAY (2.5 μM or 5 μM) for 4-day intervals between days 2 and 26, and tdTomato-positive hRGCs were quantified on day 32 using our BRN3B-P2A-tdTomato-P2A-Thy1.2 reporter line. A single time window exposure during days 2–6 produced ~1.5-fold increase in tdTomato$^+$ cells at both concentrations, with a modest but significant effect for days 6–10 at 2.5 μM; later windows were ineffective as revealed by imaging (Supplementary Fig. S3a)

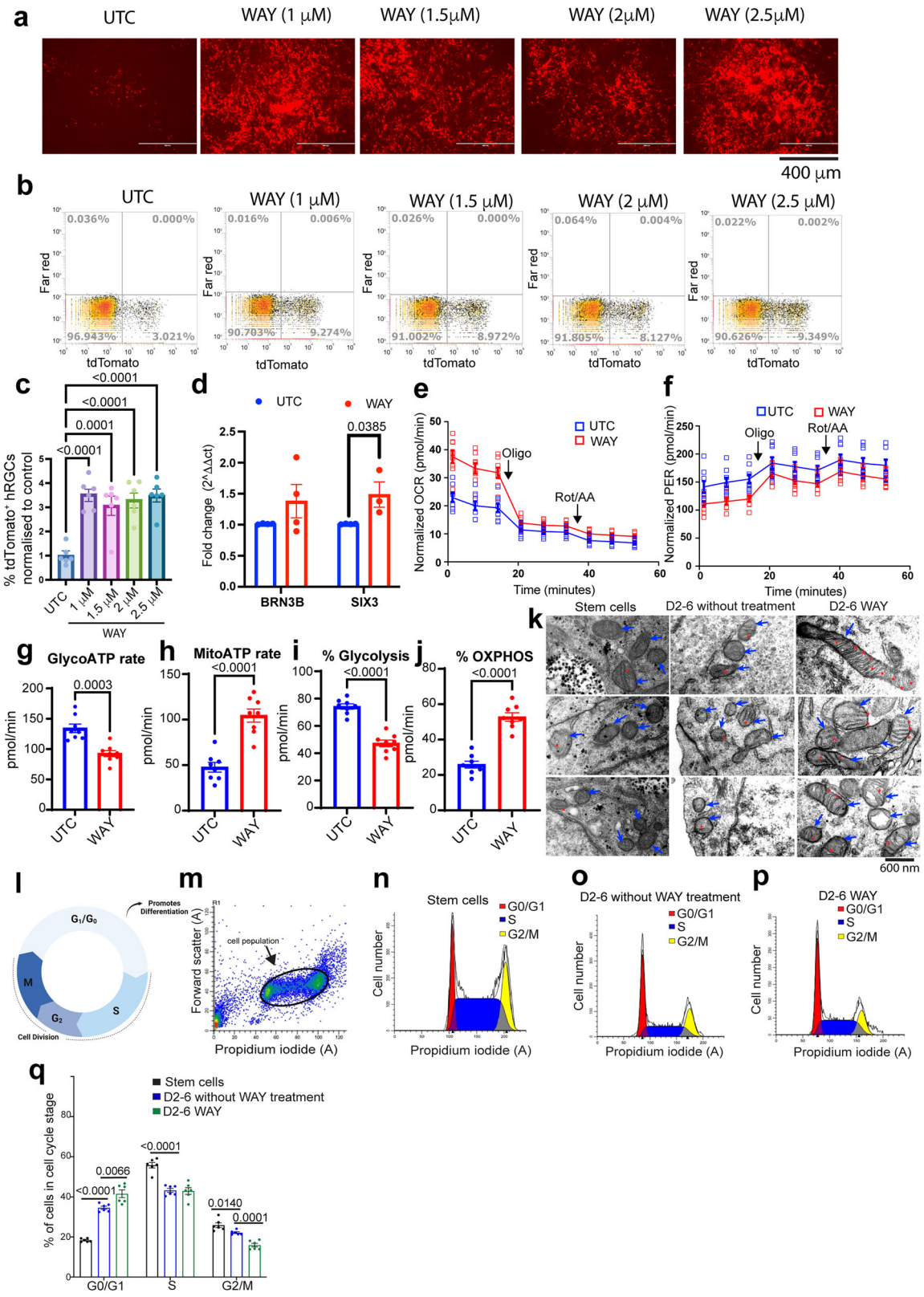

and by quantitative flow cytometry analysis (Supplementary Fig. S3b, c). Expanding the dose range (1–2.5 μM) within the days 2–6 window reproducibly elevated hRGC output irrespective of concentration, as shown by microscopy (Fig. 5a) and quantitative flow cytometry analysis (Fig. 5b, c). Molecular markers independent of tdTomato positive readouts further corroborated enhanced differentiation as early WAY treatment moderately up-regulated BRN3B and significantly upregulated SIX3 transcripts, key determinants of RGC lineage commitment[73,74] and ocular neuroectoderm patterning[75,76], respectively relative to vehicle controls (Fig. 5d).

To pinpoint the metabolic signature that underlies the permissive day 2–6 window, we interrogated bioenergetics on differentiation day 7. A 4-day pulse of WAY-100635 elevated basal oxygen-consumption rate in the

Fig. 5 | WAY-100635 reprograms metabolism to enhance hRGC differentiation. **a** Live-cell fluorescence of the BRN3B-tdTomato positive hRGCs on day 32 of differentiation, treated with the indicated concentrations of WAY during day 2–6. **b** Representative flow-cytometry plots, and **c** quantification of percentage tdTomato-positive hRGCs normalized to untreated control (UTC) differentiation from flow cytometry analysis. One-way ANOVA with Dunnett's post-hoc test; *n* (UTC, WAY 1 μM, WAY 1.5 μM, WAY 2 μM, WAY 2.5 μM) = 6 culture wells. **d** qRT-PCR analysis of the RGC transcription factors BRN3B and SIX3 after day 2−6 WAY treatment. ΔΔCt vs. GAPDH and UTC; unpaired two-tailed Student's *t* test; *n* (UTC BRN3B, WAY BRN3B, UTC SIX3) = 4 and *n* (WAY SIX3) = 3 biological replicates, each measured in three technical repeats. **e**, **f** Cell number normalized oxygen-consumption rate (OCR) and proton-efflux rate (PER) from the Seahorse ATP-rate assay on day 7 of hRGC (H7-hESC) differentiation cultures with or without WAY (5 μM) treatment (days 2–6). **g**–**j** Derived metabolic parameters - GlycoATP rate, MitoATP rate, percentage of glycolysis and OXPHOS, demonstrating a glycolysis-to-OXPHOS shift after WAY treatment. Unpaired, two-tailed Student's *t* test; *n* (UTC and WAY) = 8 culture wells. **k** Transmission-electron micrographs revealing elongated, cristae-rich mitochondria measured on day 7 post day 2–6 WAY (5 μM) treatment (23,000×; scale bar, 600 nm). Mitochondria indicated with blue arrows and cristae are with red asterisks. **l** Schematic of cell-cycle progression and G1/G0 arrest that promote differentiation. **m** Representative propidium-iodide flow cytometry scatter plot of day-7 culture indicating cell population analyzed for different cell-cycle stages. **n** Cell-cycle profiles of undifferentiated H7-hESCs, **o** day-7 untreated hRGC differentiation cells, and **p** day-7 WAY-treated cells. **q** Percentage of cells at different cell-cycle phases across conditions. Unpaired, two-tailed Student's *t* test; *n* (Stem cells, D2–6 without WAY treatment and D2–6 WAY) = 6 culture wells. Error bars are SEM. Statistical significance is indicated by exact *P* values shown between the compared groups in each panel.

seahorse ATP rate assay, which reverted to control values after electron-transport-chain blockade, indicating enhanced mitochondrial respiratory capacity (Fig. 5e). Proton-efflux rate (PER), an index of glycolytic acidification, remained significantly lower in the Day 2–6 WAY-treated cultures (Fig. 5f). Deconvolution of total ATP production confirmed a sharp decline in glycoATP and %Glycolysis (Fig. 5g, i) with a reciprocal increase in mitoATP and %OXPHOS (Fig. 5h, j). Ultrastructurally, WAY-exposed differentiation culture cells on day 7 harbored elongated mitochondria with densely packed cristae, morphological hallmarks of high-efficiency oxidative phosphorylation (Fig. 5k). Collectively, these data show that a brief pharmacologic cue enforces an early glycolysis-to-OXPHOS switch, the metabolic milestone of neuron specification[77,78], thereby mechanistically linking mitochondrial maturation to the amplified RGC yield.

Enhanced RGC differentiation indicates WAY treatment induces G_0/G_1 arrest in the progenitor stage as G_1 residency biases cells toward differentiation[79] as demonstrated in Fig. 5l. To test this, we quantified cell-cycle distribution in the RGC differentiation culture post day 2–6 WAY treatment by propidium-iodide flow cytometry method[23]. Undifferentiated hESCs were S-phase-enriched (Fig. 5m, n, q). By day 7, differentiating cultures accumulated in G_0/G_1 with concomitant reduction in the S and G2/M phase, an effect magnified by early WAY exposure (Fig. 5o–q), consistent with metabolic checkpoint-mediated exit from proliferation.

Thus, our data show a brief surge in mitochondrial biogenesis early in development triggers mitochondrial maturation, persistent OXPHOS dominance, enforces G_1 arrest, and accelerates RGC lineage specification. This result agrees with the developmental aspect of neuronal maturation as is promoted by mitochondrial maturation and OXPHOS metabolism[80]. Thus, WAY-mediated metabolic-cell-cycle coupling offers a unifying framework whereby transient pharmacologic cues can amplify stem-cell-derived RGC yield, expediting a developmental outcome and pre-installing reversible stress-resilient programs that may confer in vivo neuroprotection.

WAY protects RGC somata and distal axons with no detectable systemic toxicity

To test the in vivo efficacy of WAY, we employed two models of optic neuropathy: an acute optic nerve crush (ONC) model and a chronic high intraocular pressure (IOP) glaucoma model induced by anterior chamber microbead injection. We evaluated the in vivo efficacy of WAY using two daily intraperitoneal (i.p.) dosing regimens: a preconditioning paradigm, in which animals were treated starting 5 days prior to ONC (Day 0) and continued until sacrifice, and a post-treatment regimen designed to mimic a clinical scenario, with dosing initiated 4 h after ONC and continued daily thereafter (Fig. 6a). The 4-h post-injury timepoint was selected based on prior evidence that irreversible neurodegenerative signaling cascades are triggered within 6 h of ONC[81]. We found that the RGC count, detected by immunohistochemistry against RGC marker RNA-binding protein with multiple splicing (RBPMS) in naïve retina and ONC paradigm, consistently induces 60–80% RGC loss within one week (Fig. 6b) aligning with previous reports[82,83], providing a robust quantitative platform for evaluating neuroprotection. We see RBPMS localization both in the RGC cell body and in neurites (Fig. 6b), this localization pattern is well documented in the literature[84,85]. Daily i.p. administration of WAY, initiated prior to ONC until sacrifice, significantly preserved RGC survival at 6 days post crush (dpc) and to a lesser extent at 14 and 35 dpc (Fig. 6a, b). Post-injury treatment alone was also effective, preserving RGCs 17 days after unilateral left ONC (Fig. 6c), thereby modeling a clinically relevant therapeutic window.

To determine whether the treatment is capable of protecting axons, we quantified RGC axons using GAP-43 immunohistochemistry on transverse optic nerve sections, as it marks the active axons[86,87]. High-resolution confocal imaging with validated GAP-43 antibody[37] revealed severe degeneration in untreated ONC nerves, whereas WAY-treated animals showed robust axon protection at 14 and 25 dpc (Fig. 6d, e). Importantly, the pre-crush zone displayed a stronger GAP-43 signal than the post-crush segment, suggesting that the subset of RGCs preserved by WAY were also protected from axonal degeneration. The axon staining pattern and axonal count range by GAP-43 imaging agree to that reported in protective paradigms involving lens injury, or axon growth-promoting gene perturbations in ONC models[37,88,89].

Crucially, protected axons closely agrees with the extent of RGC soma preservation. Although RGC counts declined between 14 and 35 dpc, they remained significantly higher in WAY-treated animals than in controls (Fig. 6b). Consistently, axon counts at 14 and 25 dpc were comparable and markedly elevated relative to untreated ONC animals (Fig. 6d, e). These findings suggest that WAY not only prevents RGC body degeneration but also supports axonal protection required for optic neuropathy treatments.

To support direct target engagement of WAY with 5-HT1A in RGCs, we first confirmed receptor expression in human and mouse RGCs and assessed compound accessibility across the blood-retinal barrier. Immunofluorescence revealed strong plasma membrane localization of 5-HT1A in human stem cell-derived hRGCs (Supplementary Fig. S4a), corroborated by western blot of whole-cell lysates (Supplementary Fig. S4b). In mouse retina, confocal immunohistochemistry imaging showed robust 5-HT1A expression in RGCs marked by Tuj1 in the ganglion cell layer (GCL), which remained stable in surviving RGCs 25 days after ONC (Supplementary Fig. S4c). To quantify receptor levels, we purified RGCs from mouse retina using magnetic-activated cell sorting (MACS), the method reported to have minimal perturbation of native transcriptomic and proteomic profiles[12,90] and obtained nearly 90% purity (Supplementary Fig. S4d, e). Isolated RGCs exhibited sustained 5-HT1A expression 24 h post-ONC (Supplementary Fig. S4f), supporting continuous target availability in disease context. This data is corroborated by the single-cell RNA-seq data showing 5-HT1A expression in different RGC types[91]. WAY crosses blood-brain barrier following intraperitoneal injection in mice[92]. To assess bioavailability in retina, we performed mass spectrometry following a single intraperitoneal injection of WAY. Chromatographic peaks confirmed compound presence in both plasma and retina, with retinal levels peaking at 4 h and declining by

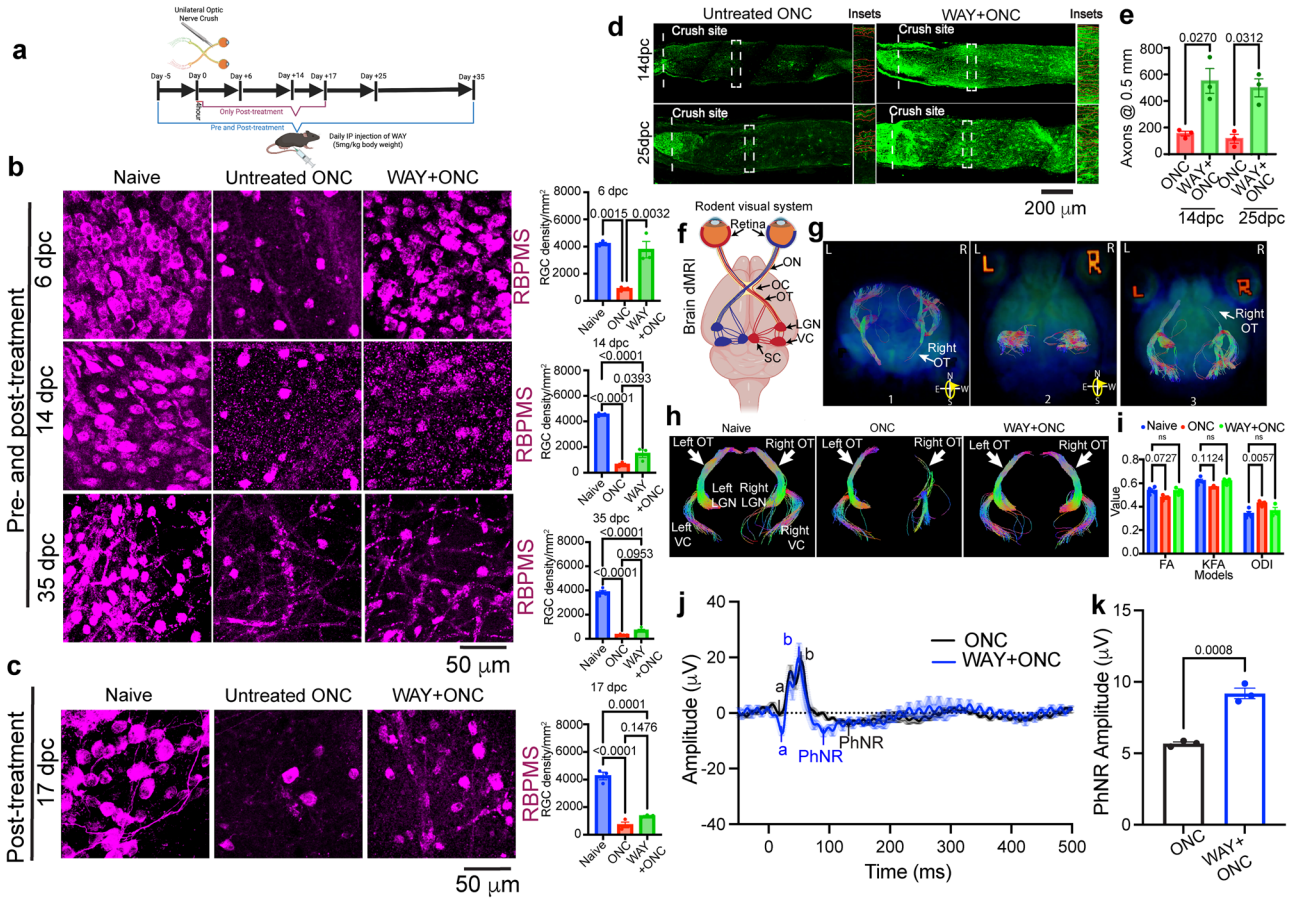

Fig. 6 | WAY-100635 preserves RGCs and protects axons after optic-nerve crush. **a** Experimental design. C57BL/6J mice received unilateral left optic-nerve crush (ONC, day 0) and daily intraperitoneal WAY (5 mg/kg) either as 5 d before optic nerve crush (pre-treatment) and continuing for 6, 14-, and 35-day post-crush (dpc) or starting 4 h post-injury (post-treatment) and continuing until the indicated dpc. **b** Representative confocal micrographs (40x/1.3 NA) of RBPMS-labeled retinal ganglion cells (RGCs) from pre-treated animals at 6, 14, and 35 dpc. RGC density was quantified by counting RBPMS$^+$ cells in four peripheral and four central retinal regions per eye, followed by averaging to obtain a single value per retina. One-way ANOVA with Tukey's; *n* (Naïve 6 dpc, ONC 6 dpc, WAY + ONC 6 dpc, Naïve 14 dpc, ONC 14 dpc, WAY + ONC 14 dpc) = 3 and (Naïve 35 dpc, ONC 35 dpc, WAY + ONC 35 dpc) = 4 mice/group. **c** Images and quantification of RGCs from ONC retina (peripheral and central) after 17 dpc when animals received daily WAY starting 4 h post-injury. One-way ANOVA with Tukey's, n (Naïve 17 dpc, ONC 17 dpc, WAY + ONC 17 dpc) = 3 mice/group. **d** GAP-43 immunostaining of longitudinal optic-nerve sections with magnified insets from crushed nerve at 14 and 25 dpc under pre-treatment condition; stitched mosaics show protected axons at 0.5 mm distal to the crush site. **e** Axon counts for (**d**); two-way ANOVA with Tukey's, *n* (ONC 14 dpc, WAY + ONC 14 dpc, ONC 25 dpc and WAY + ONC 25 dpc) = 3 mice/group. **f** Diagram of murine visual projections (~90% contralateral). **g** Diffusion-MRI tractography superimposed with the B0 image extracted from the diffusion-weighted imaging (DWI) dataset, and **h** tractography only of the optic tract (OT), lateral geniculate nucleus (LGN), and visual cortex (VC) in naïve (no treatment or injury), ONC, and WAY-treated ONC mice (pre-treatment paradigm; scan at 11–12 dpc). **i** Microstructural metrics - fractional anisotropy (FA, DTI model), kurtosis FA (KFA, DKI), and orientation-dispersion index (ODI, NODDI) for right OT region. Significant degeneration in ONC versus naïve is absent in WAY-treated mice; Two-way ANOVA with Tukey's, *n* (Naïve) = 4 and n (ONC and WAY + ONC) = 3 mice/group. **j** Representative flash-ERG traces (white flashes on a rod-saturating green background) illustrating PhNR peaks; each trace is the average of nine recordings (three technical replicates per eye, three eyes). **k** PhNR amplitude (absolute value) under the indicated conditions. Unpaired two-tailed *t*-test, Error bars are SEM; *n*, (ONC and WAY + ONC) = 3 mice/group. Statistical significance is indicated by exact *P* values shown between the compared groups in each panel.

24 h (Supplementary Fig. S5a, b), consistent with daily dosing rationale. Given the chronic nature of glaucoma, systemic safety is essential. Mice treated daily with WAY (5 mg/kg, i.p.) for 30 days exhibited no structural abnormalities in kidney or liver by hematoxylin and eosin (H&E) staining. In particular, we observed no glomerular lesions (Supplementary Fig. S5c, yellow arrows) nor necroinflammatory changes surrounding the hepatic central vein (Supplementary Fig. S5d, yellow arrows) that marks systemic toxicity[92,93]. Mice also maintained normal behavior, body weight, and activity throughout the treatment period. Together, these data confirm 5-HT1A expression in RGCs, efficient retinal penetration of WAY, and a favorable safety profile, supporting on-target efficacy in both in vitro and in vivo models.

Neurodegeneration of brain visual centers is a common and debilitating consequence of glaucoma progression[94,95], yet no existing therapy has demonstrated preservation of RGC axons into brain targets, an essential prerequisite for functional neuroprotection. To build upon our evidence of optic nerve axon protection (Fig. 6d, e), we next asked whether WAY treatment supports long-range axonal preservation into retino-recipient brain regions. We employed double-blinded diffusion MRI (dMRI) analysis to assess white matter integrity in vivo. All imaging and computational analyses were performed under identity-masked conditions. Given that ~90% of mouse RGCs project contralaterally[96] as demonstrated in Fig. 6f, we performed unilateral left ONC and focused on the right-side visual structures. In untreated animals, B0 (baseline image with no diffusion weighting) and tractography overlays confirmed optic tract (OT) degeneration predominantly in contralateral to the crushed eye, consistent with expected pathophysiology (Fig. 6g; Supplementary Movie 1). Using fully automated, unsupervised tractography algorithms[47,48], we found that ONC resulted in dramatic loss of fiber connectivity in the right OT and downstream visual centers by 11–12 days post crush. In contrast, animals treated with WAY

5 days prior to ONC until imaging exhibited robust preservation of fiber tracts along the same pathway (Fig. 6h), aligning with our earlier immunohistochemical evidence of axon protection. To quantitatively evaluate microstructural integrity, we analyzed diffusion-weighted image volumes using multiple tensor models, extracting key structural metrics including Fractional Anisotropy (FA)[44], Kurtosis Fractional Anisotropy (KFA)[45], and Orientation Dispersion Index (ODI)[46] in the right OT. FA and KFA, both indicators of axonal integrity and microstructural complexity[97] were reduced in ONC animals but preserved in the WAY-treated cohort (Fig. 6i). Conversely, ODI, which increases with disorganized fiber orientation, was elevated in ONC mice but remained low in treated animals, further indicating structural preservation (Fig. 6i).

Taken together the immunohistochemistry data of optic nerve and quantitative dMRI results of brain, it demonstrates that WAY protects proximal and distal axons of RGCs which is prerquisite to halt glaucoma progression. The RGC protection that we observed likely reflects at least in part direct engagement of 5-HT1A receptor on RGCs by WAY.

WAY preserves retinal RGC function after optic nerve injury and maintains visual acuity and contrast sensitivity in glaucoma

Building on our findings that WAY protects RGC axons, we next tested whether this structural preservation translates into functional preservation of RGC activity under neurodegenerative conditions. Using flash electroretinography (ERG) under rod-saturating green light (Diagnosys LLC), we recorded the photopic negative response (PhNR), a cone-driven RGC-specific readout, alongside the a-wave and b-wave components reflecting upstream retinal function[98–100], under the post treatment only condition (Fig. 6a, j). In ONC-injured mice, the affected eye exhibited a marked reduction in amplitude and delay in the PhNR, consistent with RGC dysfunction. Post-injury treatment with WAY significantly restored PhNR amplitude and timing (Fig. 6j, k), indicating functional rescue of RGCs even after axonal damage.

Given these robust effects in the ONC model, we next asked whether WAY preserves RGC structure and function under chronically elevated IOP, a more clinically relevant model of glaucoma. We induced unilateral ocular hypertension using microbead (MB) injection into the anterior chamber following a well-established model that elevates IOP without ischemic injury or off-target retinal damage[32,101]. Unilateral IOP elevation more closely mimics the glaucoma progression in patients as the disease often begins in one eye and then propagates to the other, a feature that has been well characterized in animal models of microbead occlusion glaucoma models[102,103]. We saw IOP elevation to ~20 mmHg on MB injected eyes and persisted for approximately 4 weeks before returning to baseline (~12 mmHg) (Fig. 7a, b), consistent with prior reports[31]. Interestingly, WAY-treated mice showed a slightly accelerated IOP elevation and resolution (Fig. 7b). However, cumulative IOP exposure over time (AUC), a stronger predictor of glaucoma risk than single IOP readings[104], was significantly higher than saline in both untreated and WAY-treated bead eyes, with no difference between the two, indicating that WAY does not affect IOP risk factor (Fig. 7b, c). Unilateral MB injection did not affect the contralateral IOP, albeit a small fluctuation on day 18 (Fig. 7d, e). Previous studies have shown that despite IOP returning to baseline within a month following a single unilateral MB injection, RGC degeneration continues for at least 8 weeks[105]. Consistent with these findings, we observed that transient IOP elevation was sufficient to cause significant RGC loss by 8 weeks in the untreated animals. Remarkably, daily treatment with WAY (6 days before MB to the day of measurements, i.p.) robustly preserved RGC density (Fig. 7f), reinforcing its neuroprotective efficacy in both acute (ONC) and chronic (IOP-induced) models of optic neuropathy. To evaluate visual function, we used the OptoMotry system to measure visual acuity and contrast sensitivity. Visual acuity declined within 7 days post-MB injection and plateaued by 4 weeks, a trajectory recapitulating adaptive changes driven by the contralateral eye[9]. WAY treatment significantly mitigated acuity loss (Fig. 7g, h), indicating functional benefit beyond anatomical protection. On the other hand, contrast sensitivity exhibited a progressive decline between days 7 and 30 in IOP-induced untreated mice, which was substantially attenuated in the WAY group (Fig. 7i).

Together with the axonal protection data, these results demonstrate that WAY confers robust and durable neuroprotection by preserving both the structure and function of RGCs across distinct models of optic neuropathy, supporting its translational potential as a glaucoma therapy.

WAY protects in vivo optic nerve function in mouse glaucoma model

The unilateral microbead model of ocular hypertension (OHT) is a well-established proxy for early glaucoma. In vivo, flash visual evoked potential (fVEP) recordings at the cortex upon light flashes at eye reliably measures the optic nerve function. This has been reported that fVEP detects intact optic nerve function for around 4 weeks post IOP elevation despite clear structural and functional changes to RGCs in the retina and their axons in optic nerve[106,107]. Around 2 weeks of unilateral IOP elevation, the RGCs in the injured eye retina (bead) shows hyperexcitability upon light stimuli that declines by week 4[9]. During this early glaucoma pathogenesis, metabolic support relocates from the fellow (uninjured) optic nerve to the stressed optic nerve as an internal rescue mechanism, even though the injured eye starts showing functional deficits by 2 weeks as anterograde transport from retina to brain declines. The metabolic translocation from the fellow optic nerve makes it vulnerable to degeneration within this early time window, setting up asymmetric but bilateral disease progression[9,103]. Thus, investigating if WAY can put a break in the early glaucoma progression will establish if the compound can serve as neuroprotective therapy.

To test whether WAY treatment preserves visual circuit during glaucoma progression, we induced unilateral ocular hypertension (left eye) by intracameral microbead injection and recorded fVEPs from the occipital cortex (Celeris, Diagnosys LLC) while alternately stimulating each eye under identical conditions (Fig. 7j, k). Our control and glaucoma waveforms; peak/trough morphology, amplitudes, and temporal profiles matched published mouse fVEP characteristics (Fig. 7l, o)[106,107].

In untreated mice, the glaucomatous eye preserved cortical responses but showed a trend of early (day 9) hyperexcitability, through increased P1-N1 peak-to-peak amplitude and a larger negative area under the curve (AUC) which remained unaffected by WAY treatment (Fig. 7l, m, n). Both untreated (red trace) and treated (green trace) glaucomatous eye (left) recordings showed broader waveforms indicating a persistent electrical conductance presumably to compensate functional deficits of RGCs under stress (Fig. 7l). Because P1-N1 amplitude and the negative AUC are proportional to the functional axons that produce cortical response[108–110], these changes are consistent with early hyperexcitability[9]. In contrast, the contralateral (right) uninjured eye of untreated mice exhibited similar optic nerve function to saline control, but remarkably the treated mice showed higher optic nerve function with higher P1-N1 amplitude (Fig. 7o, p), and significantly high negative AUC values compared to saline and untreated groups (Fig. 7o, q). This indicates that WAY treatment maintains larger number of functional axons through the optic nerve to brain of both glaucoma and fellow eye, hence can halt the bilateral glaucoma progression.

The extensive neuroprotection data presented here including human stem cell differentiated hRGCs, acute optic nerve injury, and chronic glaucoma models with no systemic toxicity, positions the 5-HT1A receptor antagonist WAY as a strong neuroprotective therapeutic candidate for optic neuropathies, including glaucoma.

Discussion

This study establishes the 5-HT1A receptor antagonist WAY as a promising therapeutic candidate for glaucoma. Integrating mechanistic insights from human pluripotent stem cell-derived RGCs (hRGCs) with in vivo anatomical and functional validation, we demonstrate that WAY initiates a multifaceted, reversible neuroprotective program, beginning with cAMP signaling, mitochondrial biogenesis and metabolic reprogramming, culminating in long-distance axonal protection and preservation of visual responses.

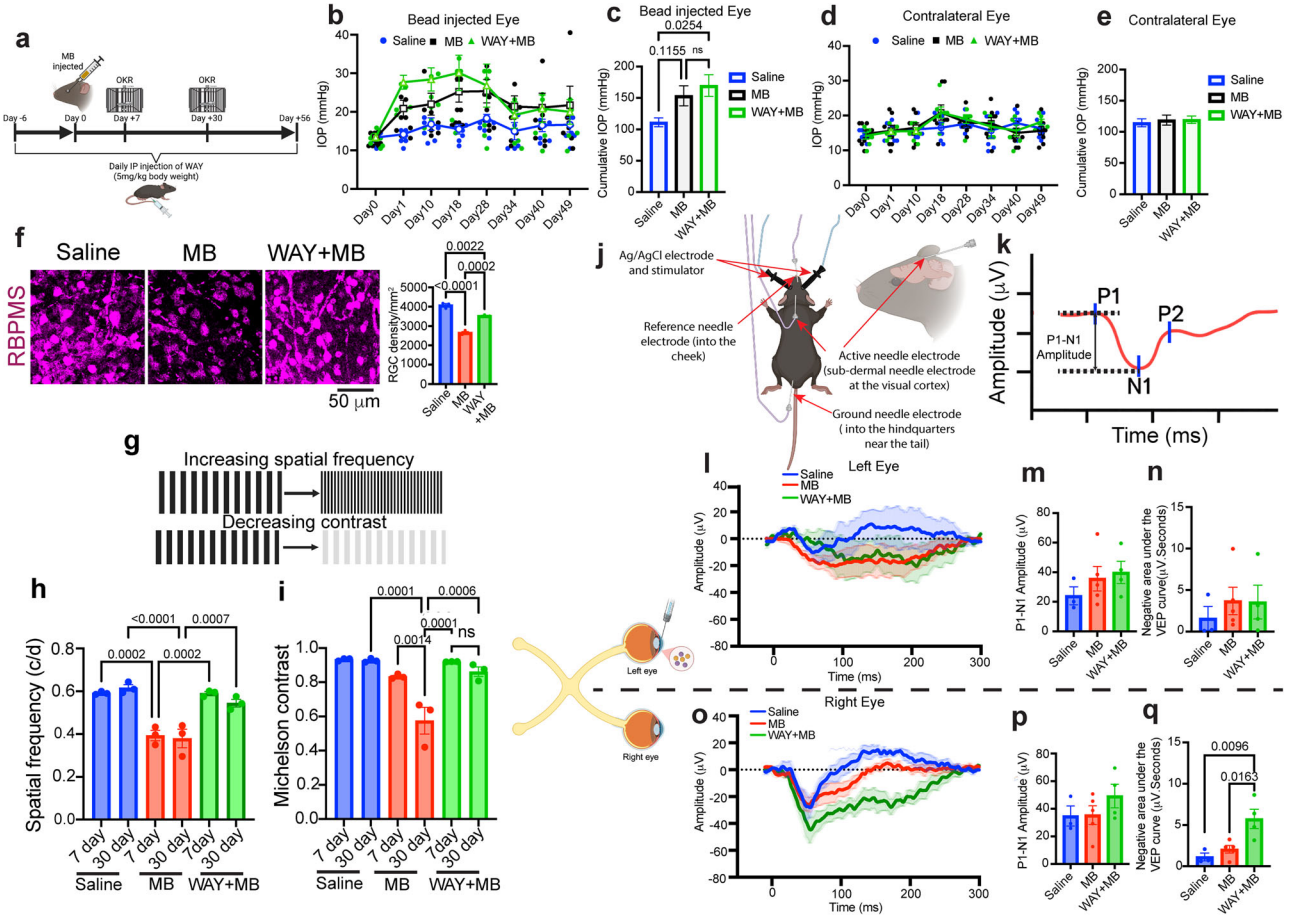

Fig. 7 | WAY-100635 protects optic nerve functions in mouse glaucoma model. **a** Schematic for chronic glaucoma model: unilateral microbead (MB) occlusion on day 0 (2 μL of 1 μm + 2 μL of 6 μm polystyrene beads) or PBS (saline) into the anterior chamber, followed by daily WAY dosing (5 mg/kg). Visual acuity (VA) and contrast sensitivity (CS) were assessed with OptoMotry on days 7 and 30 (see panels **g**–**i**). **b** Intraocular pressure (IOP) profile measured by rebound tonometry: sustained elevation for around 4 weeks with subsequent return toward baseline in bead injected eye, **d** and contralateral eye. **c** Time integrated IOP exposure referred to as cumulative IOP in the bead injected left eye, and **e** contralateral right eye is represented as area under curve (AUC). The AUC panel summarizes group-level cumulative IOP burden, not per-animal AUC. One-way ANOVA with Tukey's; *n* (Saline) = 6, *n* (MB) = 8, *n* (MB + WAY) = 7 (up to day 18), 6 (rest of the time-course). **f** Representative confocal images of RBPMS-immunolabeled RGCs 56 days after MB induction ± WAY or in saline control. RGC density (cells/mm^2) was quantified by sampling four peripheral and four central retinal fields from the indicated retina, averaged to obtain a single density measurement per retina. One-way ANOVA with Tukey's post-hoc; *n* (Saline, MB and WAY + MB) = 3 mice/group. **g**–**i** Functional vision outcomes. **g** Cartoon, and **h** quantifications describe the measurement of VA (cycles/deg) determined by head-tracking to drifting gratings of increasing spatial frequency. **g**, **i** describes contrast sensitivity measured by head-tracking to decreasing contrast of fixed frequency. Measurements were performed under blinded conditions for both clockwise and counter-clockwise rotation. Two-way ANOVA with Tukey's correction; *n* (Saline 7day, MB 7day, WAY + MB 7day, Saline 30day, MB 30day and WAY + MB 30day) = 3 mice/group. Data are mean ± SEM. **j** Schematic diagram of the experimental setup for VEP recordings showing electrode placement: two Ag/AgCl electrodes (stimulator and reference), a reference needle electrode inserted into the cheek, an active subdermal needle electrode positioned over the visual cortex, and a ground electrode placed in the hindquarters near the tail. **k** Representative VEP waveforms showing characteristic P1, N1, and P2 peaks. **l**, **o** Representative flash VEP traces from each experimental group; each trace represents the average response of each group. **m**, **p** Quantification of P1-N1 peak-to-peak amplitude absolute values under the indicated experimental conditions. **n**, **q** Corresponding negative area under the curve (AUC) measurements representing the negative-going VEP component. Statistical significance was determined by one-way ANOVA with Tukey's post hoc correction; *n* (Saline) = 3, *n* (MB) = 5 and *n* (MB + WAY) = 4 mice per group. Statistical significance is indicated by exact *P* values shown between the compared groups in each panel.

Glaucoma pathogenesis is axogenic, with RGC axons undergoing varying stages of degeneration[5,111]. Although some RGCs progress to irreversible damage, others remain at early stages, offering a critical opportunity for neuroprotective intervention. In experimental microbead occlusion glaucoma model, this has been shown that RGC loss continues long after eye pressure becomes normal[105], thus indicate if diagnosed early, a neuroprotection approach can protect these neurons. Functional deficits of RGCs often precede structural damage in glaucoma, explaining why significant vision loss occurs even with minimal RGC body loss, as demonstrated in non-human primate models[111,112]. Currently, there is no safe pharmacological intervention that can reversibly activate multiple RGC protective pathways for long-term glaucoma therapy, without the risks associated with constitutive gene expression or suppression (e.g., via viral delivery)[113].

Our data reveal a dual and stage-specific benefit of WAY-mediated metabolic reprogramming. Early treatment during the progenitor phase enhances mitochondrial maturation, promotes oxidative phosphorylation (OXPHOS), accelerates cell-cycle exit, and increases the yield of differentiated RGCs (Fig. 5). In contrast, treating differentiated WT or OPTN^{E50K} hRGCs restores mitochondrial health but favors a shift toward aerobic glycolysis (Fig. 4). These distinct metabolic outcomes carry two important implications.

Metabolic reprograming with enhanced mitochondria dependent metabolism are important for stem cell differentiations including

cardiomyocytes, and neurons[80,114]. However, we still lack a safe pharmacological compound that will achieve this goal to overcome the translational barrier. First, pharmacologically enhancing RGC differentiation with a safe compound like WAY could transform stem cell-based cell replacement strategies for late-stage glaucoma. A key limitation in such therapies is generating sufficient numbers of lineage-committed RGCs while minimizing undifferentiated or proliferative cells that carry teratoma risk when transplanted[115,116]. Our finding that WAY-treated progenitors exit the cell cycle earlier and yield more RGCs suggests that fewer, metabolically primed progenitors may be sufficient for transplantation, reducing tumorigenic risk while improving therapeutic efficiency. In addition to cell replacement strategies, reinforcing RGC differentiation programs can itself be neuroprotective. Transcription factors ATOH7 and POU4F2/Brn3b that drive RGC specification during development are upregulated after optic nerve injury and linked to enhanced RGC survival[71,117]. Thus, approaches that boost RGC differentiation such as by WAY treatment that we have discovered here may provide complementary neuroprotection alongside its direct metabolic reprogramming effects. Second, in differentiated RGCs, the induction of healthy mitochondria alongside an aerobic glycolytic shift appears tailored for functional and/or structural protection of axons. Notably, healthy mitochondria can support aerobic glycolysis without promoting excessive OXPHOS, thereby limiting oxidative stress[118,119]. Aerobic glycolysis does not just play a backup ATP resource, but it feeds lipid and protein synthesis needed for cellular homeostasis, and sustained axonal-synaptic function[120,121],. As such, brain imaging of Alzheimer patients showed regions with decreased aerobic glycolysis correlates with increased neurodegenerative amyloid plaque formation[122]; and in ONC mouse model, induction of aerobic glycolysis promoted RGC protection[69]. It seems paradoxical as the lactate biproduct of aerobic glycolysis can increase acidity of the tissue that can be toxic in long run. However, lactate can be beneficial as a small fraction crosses the blood-brain barrier and is cleared, whereas the remainder is oxidized and serves as a supplementary fuel alongside glucose[123,124]. Moreover, WAY treatment to hRGCs shows reversible activations, making a constitutive activation of aerobic glycolysis unlikely. Thus, in vivo, particularly in ONC, WAY treatment likely tunes metabolic reprogramming toward aerobic glycolysis to support RGC protection. Although, the protection is reduced beyond one week, but this is typical for ONC. For example, retinal BDNF extends median RGC survival for about one week post ONC, which diminishes by 2–4 weeks, and systemic anti-inflammatory drug minocycline protects until 1 week but not thereafter, reflecting the model's severity and irreversible damage rather than lack of efficacy[125,126]. The other critical aspect of WAY treatment is the protection of proximal (Fig. 6d, e) and distal axons (Fig. 6f–i) in the optic nerve and brain, respectively, which is required for successful glaucoma therapy. Long-distance axon protection can also be supported by promoting aerobic glycolysis as it provides critical building blocks for maintaining the axonal structure and function[120,121].

WAY treatment produced axonal protection and preserved retinal function (PhNR) in the acute ONC model. In the microbead-induced glaucoma model, it preserved RGC survival, visual acuity, and retina-to-cortex signal propagation as detected by fVEP, demonstrating protected RGC axonal function from retina to brain via the optic nerve. Consistent with the unilateral-IOP trajectory[9], the injured eye exhibited early moderate hyperexcitability. Notably, WAY significantly enhanced the fellow optic nerve response, suggesting restoration of metabolic balance across both optic nerves so the fellow pathway need not to compensate for the injured one as described previously[9,103]. In the bead eye, the broader negative waveform despite a stronger response indicates prolonged axonal activation and/or reduced inhibitory shaping, likely a compensatory adaptation under elevated IOP, one that may be further improved with concurrent IOP-lowering therapy.

Together, these results position WAY as a context-dependent modulator of RGC metabolism, promoting OXPHOS and differentiation in progenitors while enabling glycolysis-driven anabolic growth and axonal remodeling in mature neurons. This dual mechanism supports both the enhanced differentiation of RGCs for regenerative medicine and protection of cell body and long-distance axonal structure-function, offering a powerful strategy for preserving vision in glaucoma.

While our findings support the 5-HT1A receptor antagonist WAY as a promising neuroprotective agent for glaucoma, prior studies have reported protective effects of 5-HT1A agonists such as 8-OH-DPAT (DPAT), leading to apparent discrepancies in the field[127,128]. These differences likely stem from context-dependent effects of 5-HT1A signaling on RGC physiology and survival under varying experimental conditions.

Mechanistically, 5-HT1A is a Gi/o-coupled GPCR whose activation suppresses adenylyl cyclase and reduces intracellular cAMP. In contrast, antagonism by WAY relieves this inhibition, leading to cAMP elevation, a second messenger known to support neuronal survival and axonal regeneration[55,56,129]. Our data demonstrate that WAY treatment reversibly increases cAMP, enhances mitochondrial biogenesis, and reduces apoptosis in $OPTN^{E50K}$ and WT hRGCs. Conversely, DPAT treatment decreased cAMP (Fig. 1) and increased apoptosis in the $OPTN^{E50K}$ hRGCs (Fig. 3j), suggesting an opposing, contextually maladaptive effect under disease-relevant conditions. Interestingly, selective seretonin reuptake inhibitors (SSRIs), which increase serotonin concentration in synaptic cleft, are linked to higher glaucoma risk[130], likely due to overstimulation of 5-HT1A receptors. Several factors may account for the divergence in reported effects. First, it has been shown that enhanced RGC excitability within 2 weeks of elevated IOP is protective, which declines after 4 weeks with axonal degeneration[9,103,131]. However, the above studies show that while DPAT suppresses RGC excitation at 4 weeks of IOP elevation, WAY rescues it[127,128], which supports WAY as protective and DPAT as degenerative. This suggests DPAT's protective effects may be indirect, potentially via lowering IOP as was observed in rabbits[132]. However, WAY in our hand, did not significantly affect IOP in mouse MB induced glaucoma model, indicating its direct neuroprotective effect. Another anomaly may arise from the retrograde labeling method used in detecting RGC protection. The authors used fluorogold labeling to assess RGC survival[128], but this method detects retrograde transport defects (brain to eye) rather than true cell survival[5].

Taken together, while 5-HT1A agonists may offer transient benefits under specific conditions, our mechanistic and functional data favor 5-HT1A antagonism via WAY as a more consistent and directly protective strategy for RGC survival and optic nerve function in glaucoma.

Glaucoma produces a compartmentalized pattern of RGC injury in which axons at the optic-nerve head experience localized trauma due to high IOP, inducing axonal degeneration a process known as Wallerian degeneration which leads to transport failure and "dying-back" distal axonopathy[133,134]. Somal apoptosis follows axonal degeneration via partly distinct programs, while soma rescue by suppressing apoptosis does not fully prevent axon loss[134]. The central driver of Wallerian degeneration is the activation of Sterile alpha and TIR motif containing 1 (SARM1) protein that breaks down NAD+ to cause bioenergetic failure leading to axon degeneration[135,136]. NAD+ is reduced to NADH in glycolysis, which fuels OXPHOS steps in mitochondria. Thus, our discovery that WAY treatment reprograms RGC metabolism to aerobic glycolysis is significant as it can regain the NAD + /NADH and hence bioenergetic balance in the axons. Future studies would require resolving if WAY treatment mitigates SARM1 activity in glaucomatous or ONC axons and regain the NAD + /NADH metabolic balance to attenuate Wallerian degeneration.

Our findings reveal that WAY's neuroprotective effect extends beyond metabolic reprogramming and likely involves a convergence of pro-survival and regenerative signaling cascades downstream of 5-HT1A antagonism. Future studies need to resolve the RGC protection versus regeneration effect of WAY and involved downstream signaling pathways. The downstream signaling cascade may involve cAMP regulation of CREB, CaMKII, and SIRT1 factors that have known RGC protective effect[137–139]. RGC axon regeneration can be studied by axon tracing over time using intravitreal injection of anterograde tracer cholera toxin B (CTB) subunit, and by optic-nerve profiling with axon counts and myelination status on cross-sections sampled at defined distances from the optic-nerve head, using

paraphenylenediamine (PPD) or osmium staining[11,140–142]. Additionally, although our analyses focused on RGC-intrinsic effects, the contributions of non-neuronal cell types including astrocytes, microglia, and vascular cells are not yet defined. These populations could modulate inflammation, provide metabolic support, or secrete trophic factors that enhance WAY's efficacy in vivo. Ultimately, a deeper understanding of the molecular and cellular landscape engaged by WAY will guide rational combination therapies and inform translational strategies for optic nerve protection, and/or regeneration more broadly.

This study identifies WAY-100635 as a pharmacological agent that restores mitochondrial homeostasis, promotes RGC differentiation, and preserves visual system integrity across multiple models of glaucoma. By antagonizing 5-HT1A receptor, WAY engages a cascade of neuroprotective mechanisms that unify metabolic support, transcriptional plasticity (PGC-1α), and visual circuit. These findings open avenues for repurposing serotonergic modulators in neurodegenerative diseases and highlight the power of targeting intrinsic neuronal pathways for durable vision preservation.

Data availability

The resources used in this study have been detailed in the method and Supplemental table 1, and source data are available in Supplementary Data 2. Requests for further information and resources should be directed to and will be fulfilled by the lead contact, Arupratan Das (arupdas@iu.edu). All uncropped images for western blots are presented in the Supplementary Fig. 6 and flow cytometry gating steps are presented in the Supplementary Fig. 7.

Received: 6 July 2025; Accepted: 5 March 2026;
Published online: 02 April 2026

References

1. Quigley, H. A. Understanding glaucomatous optic neuropathy: the synergy between clinical observation and investigation. *Annu Rev. Vis. Sci.* **2**, 235–254 (2016).
2. Das, A. & Imanishi, Y. Drug discovery strategies for inherited retinal degenerations. *Biology* **11**, 1338 (2022).
3. Susanna, R. Jr, De Moraes, C. G., Cioffi, G. A. & Ritch, R. Why do people (still) go blind from glaucoma?. *Transl. Vis. Sci. Technol.* **4**, 1 (2015).
4. Sommer, A. et al. Relationship between intraocular pressure and primary open angle glaucoma among white and black Americans. The Baltimore Eye Survey. *Arch. Ophthalmol.* **109**, 1090–1095 (1991).
5. Calkins, D. J. Critical pathogenic events underlying progression of neurodegeneration in glaucoma. *Prog. Retin Eye Res.* **31**, 702–719 (2012).
6. Zhang, Z. Q., Xie, Z., Chen, S. Y. & Zhang, X. Mitochondrial dysfunction in glaucomatous degeneration. *Int. J. Ophthalmol.* **16**, 811–823 (2023).
7. Baltan, S. et al. Metabolic vulnerability disposes retinal ganglion cell axons to dysfunction in a model of glaucomatous degeneration. *J. Neurosci.* **30**, 5644–5652 (2010).
8. Crish, S. D. & Calkins, D. J. Central visual pathways in glaucoma: evidence for distal mechanisms of neuronal self-repair. *J. Neuroophthalmol.* **35**, S29–S37 (2015).
9. Risner, M. L., Pasini, S., Cooper, M. L., Lambert, W. S. & Calkins, D. J. Axogenic mechanism enhances retinal ganglion cell excitability during early progression in glaucoma. *Proc. Natl. Acad. Sci. USA* **115**, E2393–e2402 (2018).
10. Au, N. P. B. et al. A small molecule M1 promotes optic nerve regeneration to restore target-specific neural activity and visual function. *Proc. Natl. Acad. Sci. USA* **119**, e2121273119 (2022).
11. Cartoni, R. et al. The mammalian-specific protein Armcx1 regulates mitochondrial transport during axon regeneration. *Neuron* **92**, 1294–1307 (2016).
12. Quintero, H. et al. Restoration of mitochondria axonal transport by adaptor Disc1 supplementation prevents neurodegeneration and rescues visual function. *Cell Rep.* **40**, 111324 (2022).
13. Liu, D. et al. Optineurin-facilitated axonal mitochondria delivery promotes neuroprotection and axon regeneration. *Nat. Commun.* **16**, 1789 (2025).
14. Harder, J. M. et al. Disturbed glucose and pyruvate metabolism in glaucoma with neuroprotection by pyruvate or rapamycin. *Proc. Natl. Acad. Sci. USA* **117**, 33619–33627 (2020).
15. Tribble et al. Nicotinamide provides neuroprotection in glaucoma by protecting against mitochondrial and metabolic dysfunction. *Redox Biol.* **43**, 101988 (2021).
16. Williams, P. A. et al. Vitamin B(3) modulates mitochondrial vulnerability and prevents glaucoma in aged mice. *Science* **355**, 756–760 (2017).
17. Gozlan, H., Thibault, S., Laporte, A. M., Lima, L. & Hamon, M. The selective 5-HT1A antagonist radioligand [3H]WAY 100635 labels both G-protein-coupled and free 5-HT1A receptors in rat brain membranes. *Eur. J. Pharm.* **288**, 173–186 (1995).
18. Forster, E. A. et al. A pharmacological profile of the selective silent 5-HT1A receptor antagonist, WAY-100635. *Eur. J. Pharm.* **281**, 81–88 (1995).
19. Rezaie, T. et al. Adult-onset primary open-angle glaucoma caused by mutations in optineurin. *Science* **295**, 1077–1079 (2002).
20. Surma, M. et al. Enhanced mitochondrial biogenesis promotes neuroprotection in human pluripotent stem cell derived retinal ganglion cells. *Commun. Biol.* **6**, 218 (2023).
21. Sluch, V. M. et al. Enhanced Stem Cell Differentiation and Immunopurification of Genome Engineered Human Retinal Ganglion Cells. *Stem Cells Transl. Med.* **6**, 1972–1986 (2017).
22. Das, A., Bell, C. M., Berlinicke, C. A., Marsh-Armstrong, N. & Zack, D. J. Programmed switch in the mitochondrial degradation pathways during human retinal ganglion cell differentiation from stem cells is critical for RGC survival. *Redox Biol.* **34**, 101465 (2020).
23. Sardar Pasha, S. P. B. et al. Ref-1/APE1 inhibition with novel small molecules blocks ocular neovascularization. *J. Pharm. Exp. Ther.* **367**, 108–118 (2018).
24. Baine, R. E. et al. Noxious stimulation induces acute hemorrhage and impairs long-term recovery after spinal cord injury (SCI) in female rats: evidence estrous cycle may have a modulatory effect. *Neurotrauma Rep.* **3**, 70–86 (2022).
25. Shanley, M. R. et al. Estrous cycle mediates midbrain neuron excitability altering social behavior upon stress. *J. Neurosci.* **43**, 736–748 (2023).
26. Shaw, G. A. Mitochondria as the target for disease related hormonal dysregulation. *Brain Behav. Immun. Health* **18**, 100350 (2021).
27. Kimball, E. et al. The role of aquaporin-4 in optic nerve head astrocytes in experimental glaucoma. *PLOS One* **16**, e0244123 (2021).
28. Quillen, S. et al. Astrocyte responses to experimental glaucoma in mouse optic nerve head. *PLOS One* **15**, e0238104 (2020).
29. Feng, Q., Wong, K. A. & Benowitz, L. I. Full-length optic nerve regeneration in the absence of genetic manipulations. *JCI Insight* **8**, e164579 (2023).
30. Lindborg, J. A. et al. Optic nerve regeneration screen identifies multiple genes restricting adult neural repair. *Cell Rep.* **34**, 108777 (2021).
31. Madhoun, S. et al. Effects of experimental glaucoma in Lama1(nmf223) mutant mice. *Exp. Eye Res.* **226**, 109341 (2023).
32. Korneva, A. et al. A method to quantify regional axonal transport blockade at the optic nerve head after short term intraocular pressure elevation in mice. *Exp. Eye Res.* **196**, 108035 (2020).
33. Takita, S. et al. Rhodopsin mislocalization drives ciliary dysregulation in a novel autosomal dominant retinitis pigmentosa knock-in mouse model. *FASEB J.* **38**, e23606 (2024).

34. Benowitz, L. I., Apostolides, P. J., Perrone-Bizzozero, N., Finklestein, S. P. & Zwiers, H. Anatomical distribution of the growth-associated protein GAP-43/B-50 in the adult rat brain. *J. Neurosci.* **8**, 339–352 (1988).
35. Xie, L. et al. Monocyte-derived SDF1 supports optic nerve regeneration and alters retinal ganglion cells' response to Pten deletion. *Proc. Natl. Acad. Sci. USA* **119**, e2113751119 (2022).
36. Peterson, S. L. et al. Retinal ganglion cell axon regeneration requires complement and myeloid cell activity within the optic nerve. *J. Neurosci.* **41**, 8508–8531 (2021).
37. Leon, S., Yin, Y., Nguyen, J., Irwin, N. & Benowitz, L. I. Lens injury stimulates axon regeneration in the mature rat optic nerve. *J. Neurosci.* **20**, 4615–4626 (2000).
38. Prusky, G. T., Alam, N. M. & Douglas, R. M. Enhancement of vision by monocular deprivation in adult mice. *J. Neurosci.* **26**, 11554–11561 (2006).
39. Prusky, G. T., Alam, N. M., Beekman, S. & Douglas, R. M. Rapid quantification of adult and developing mouse spatial vision using a virtual optomotor system. *Invest. Ophthalmol. Vis. Sci.* **45**, 4611–4616 (2004).
40. Veraart, J. et al. Denoising of diffusion MRI using random matrix theory. *Neuroimage* **142**, 394–406 (2016).
41. Kellner, E., Dhital, B., Kiselev, V. G. & Reisert, M. Gibbs-ringing artifact removal based on local subvoxel-shifts. *Magn. Reson. Med.* **76**, 1574–1581 (2016).
42. Andersson, J. L. R. & Sotiropoulos, S. N. An integrated approach to correction for off-resonance effects and subject movement in diffusion MR imaging. *Neuroimage* **125**, 1063–1078 (2016).
43. Tournier, J. D. et al. MRtrix3: a fast, flexible and open software framework for medical image processing and visualisation. *Neuroimage* **202**, 116137 (2019).
44. Basser, P. J., Mattiello, J. & LeBihan, D. MR diffusion tensor spectroscopy and imaging. *Biophys. J.* **66**, 259–267 (1994).
45. Jensen, J. H., Helpern, J. A., Ramani, A., Lu, H. & Kaczynski, K. Diffusional kurtosis imaging: the quantification of non-gaussian water diffusion by means of magnetic resonance imaging. *Magn. Reson. Med.* **53**, 1432–1440 (2005).
46. Zhang, H., Schneider, T., Wheeler-Kingshott, C. A. & Alexander, D. C. NODDI: practical in vivo neurite orientation dispersion and density imaging of the human brain. *Neuroimage* **61**, 1000–1016 (2012).
47. Tournier, J. D., Calamante, F. & Connelly, A. Robust determination of the fibre orientation distribution in diffusion MRI: Non-negativity constrained super-resolved spherical deconvolution. *NeuroImage* **35**, 1459–1472 (2007).
48. Smith, R. E., Tournier, J.-D., Calamante, F. & Connelly, A. SIFT: Spherical-deconvolution informed filtering of tractograms. *NeuroImage* **67**, 298–312 (2013).
49. Xiao, B., Deng, X., Zhou, W. & Tan, E. K. Flow cytometry-based assessment of mitophagy using MitoTracker. *Front. Cell Neurosci.* **10**, 76 (2016).
50. Pereiro, X., Miltner, A. M., La Torre, A. & Vecino, E. Effects of adult müller cells and their conditioned media on the survival of stem cell-derived retinal ganglion cells. *Cells* **9**, 1759 (2020).
51. Ieni, J. R. & Meyerson, L. R. The 5-HT1A receptor probe [3H]8-OH-DPAT labels the 5-HT transporter in human platelets. *Life Sci.* **42**, 311–320 (1988).
52. Nikolaus, S. et al. The 5-HT(1A) receptor agonist 8-OH-DPAT modulates motor/exploratory activity, recognition memory and dopamine transporter binding in the dorsal and ventral striatum. *Neurobiol. Learn Mem.* **205**, 107848 (2023).
53. Raymond, J. R., Mukhin, Y. V., Gettys, T. W. & Garnovskaya, M. N. The recombinant 5-HT1A receptor: G protein coupling and signalling pathways. *Br. J. Pharm.* **127**, 1751–1764 (1999).
54. Reggiani, J. D. S. et al. Brainstem serotonin neurons selectively gate retinal information flow to thalamus. *Neuron* **111**, 711–726.e711 (2023).
55. Boczek, T. et al. cAMP at perinuclear mAKAPα signalosomes is regulated by local Ca(2+) signaling in primary hippocampal neurons. *eNeuro* **8**, ENEURO.0298-20.2021 (2021).
56. Corredor, R. G. et al. Soluble adenylyl cyclase activity is necessary for retinal ganglion cell survival and axon growth. *J. Neurosci.* **32**, 7734–7744 (2012).
57. Farde, L. et al. PET-characterization of [carbonyl-11C]WAY-100635 binding to 5-HT1A receptors in the primate brain. *Psychopharmacology* **133**, 196–202 (1997).
58. Marona-Lewicka, D. & Nichols, D. E. WAY 100635 produces discriminative stimulus effects in rats mediated by dopamine D(4) receptor activation. *Behav. Pharm.* **20**, 114–118 (2009).
59. Chemel, B. R., Roth, B. L., Armbruster, B., Watts, V. J. & Nichols, D. E. WAY-100635 is a potent dopamine D4 receptor agonist. *Psychopharmacology* **188**, 244–251 (2006).
60. Petelák, A., Lambert, N. A. & Bondar, A. Serotonin 5-HT(7) receptor slows down the G(s) protein: a single molecule perspective. *Mol. Biol. Cell* **34**, br14 (2023).
61. Sprouse, J., Reynolds, L., Li, X., Braselton, J. & Schmidt, A. 8-OH-DPAT as a 5-HT7 agonist: phase shifts of the circadian biological clock through increases in cAMP production. *Neuropharmacology* **46**, 52–62 (2004).
62. Xing, F. et al. The anti-Warburg effect elicited by the cAMP-PGC1α pathway drives differentiation of glioblastoma cells into astrocytes. *Cell Rep.* **18**, 468–481 (2017).
63. Schinder, A. F., Olson, E. C., Spitzer, N. C. & Montal, M. Mitochondrial dysfunction is a primary event in glutamate neurotoxicity. *J. Neurosci.* **16**, 6125–6133 (1996).
64. VanderWall, K. B. et al. Retinal ganglion cells with a glaucoma OPTN(E50K) mutation exhibit neurodegenerative phenotypes when derived from three-dimensional retinal organoids. *Stem Cell Rep.* **15**, 52–66 (2020).
65. Soni, A. et al. Improved method for efficient generation of functional neurons from murine neural progenitor cells. *Cells* **10**, 1894 (2021).
66. Mossink, B. et al. Human neuronal networks on micro-electrode arrays are a highly robust tool to study disease-specific genotype-phenotype correlations in vitro. *Stem Cell Rep.* **16**, 2182–2196 (2021).
67. Odawara, A., Saitoh, Y., Alhebshi, A. H., Gotoh, M. & Suzuki, I. Long-term electrophysiological activity and pharmacological response of a human induced pluripotent stem cell-derived neuron and astrocyte co-culture. *Biochem. Biophys. Res. Commun.* **443**, 1176–1181 (2014).
68. Tezel, G. Oxidative stress in glaucomatous neurodegeneration: mechanisms and consequences. *Prog. Retin Eye Res.* **25**, 490–513 (2006).
69. Zhu, J., Li, P., Zhou, Y. G. & Ye, J. Altered energy metabolism during early optic nerve crush injury: implications of warburg-like aerobic glycolysis in facilitating retinal ganglion cell survival. *Neurosci. Bull.* **36**, 761–777 (2020).
70. Goyal, M. S. et al. Brain aerobic glycolysis and resilience in Alzheimer disease. *Proc. Natl. Acad. Sci. USA* **120**, e2212256120 (2023).
71. Jacobi, A. et al. Overlapping transcriptional programs promote survival and axonal regeneration of injured retinal ganglion cells. *Neuron* **110**, 2625–2645.e2627 (2022).
72. Folmes, C. D. & Terzic, A. Energy metabolism in the acquisition and maintenance of stemness. *Semin. Cell Dev. Biol.* **52**, 68–75 (2016).
73. Qiu, F., Jiang, H. & Xiang, M. A comprehensive negative regulatory program controlled by Brn3b to ensure ganglion cell specification from multipotential retinal precursors. *J. Neurosci.* **28**, 3392 (2008).
74. Miltner, A. M. et al. A novel reporter mouse uncovers endogenous Brn3b expression. *Int. J. Mol. Sci.* **20**, 2903 (2019).
75. Heavner, W. & Pevny, L. Eye development and retinogenesis. *Cold Spring. Harb. Perspect. Biol.* **4**, a008391 (2012).

76. Samuel, A. et al. Six3 regulates optic nerve development via multiple mechanisms. *Sci. Rep.* **6**, 20267 (2016).
77. Zheng, X. et al. Metabolic reprogramming during neuronal differentiation from aerobic glycolysis to neuronal oxidative phosphorylation. *Elife* **5**, e13374 (2016).
78. Zhou, W. et al. TIGAR promotes neural stem cell differentiation through acetyl-CoA-mediated histone acetylation. *Cell Death Dis.* **10**, 198 (2019).
79. Pauklin, S. & Vallier, L. The cell-cycle state of stem cells determines cell fate propensity. *Cell* **155**, 135–147 (2013).
80. Iwata, R. et al. Mitochondria metabolism sets the species-specific tempo of neuronal development. *Science* **379**, eabn4705 (2023).
81. Lukas, T. J., Wang, A. L., Yuan, M. & Neufeld, A. H. Early cellular signaling responses to axonal injury. *Cell Commun. Signal* **7**, 5 (2009).
82. Sánchez-Migallón, M. C., Valiente-Soriano, F. J., Nadal-Nicolás, F. M., Vidal-Sanz, M. & Agudo-Barriuso, M. Apoptotic retinal ganglion cell death after optic nerve transection or crush in mice: delayed rgc loss with BDNF or a caspase 3 inhibitor. *Invest. Ophthalmol. Vis. Sci.* **57**, 81–93 (2016).
83. Leung, C. K. et al. Longitudinal profile of retinal ganglion cell damage after optic nerve crush with blue-light confocal scanning laser ophthalmoscopy. *Invest. Ophthalmol. Vis. Sci.* **49**, 4898–4902 (2008).
84. Kwong, J. M., Caprioli, J. & Piri, N. RNA binding protein with multiple splicing: a new marker for retinal ganglion cells. *Invest. Ophthalmol. Vis. Sci.* **51**, 1052–1058 (2010).
85. Pereiro, X., Ruzafa, N., Urcola, J. H., Sharma, S. C. & Vecino, E. Differential distribution of RBPMS in pig, rat, and human retina after damage. *Int. J. Mol. Sci.* **21**, 9330 (2020).
86. Hoffman, P. N. Expression of GAP-43, a rapidly transported growth-associated protein, and class II beta tubulin, a slowly transported cytoskeletal protein, are coordinated in regenerating neurons. *J. Neurosci.* **9**, 893–897 (1989).
87. Benowitz, L., Shashoua, V. & Yoon, M. Specific changes in rapidly transported proteins during regeneration of the goldfish optic nerve. *J. Neurosci.* **1**, 300–307 (1981).
88. Li, Y. et al. Mobile zinc increases rapidly in the retina after optic nerve injury and regulates ganglion cell survival and optic nerve regeneration. *Proc. Natl. Acad. Sci. USA* **114**, E209–e218 (2017).
89. Cheng, Y. et al. Transcription factor network analysis identifies REST/NRSF as an intrinsic regulator of CNS regeneration in mice. *Nat. Commun.* **13**, 4418 (2022).
90. Shekhar, K., Whitney, I. E., Butrus, S., Peng, Y.-R. & Sanes, J. R. Diversification of multipotential postmitotic mouse retinal ganglion cell precursors into discrete types. *eLife* **11**, e73809 (2022).
91. Tran, N. M. et al. Single-cell profiles of retinal ganglion cells differing in resilience to injury reveal neuroprotective genes. *Neuron* **104**, 1039–1055.e1012 (2019).
92. Markowitz, G. S., Bomback, A. S. & Perazella, M. A. Drug-induced glomerular disease: direct cellular injury. *Clin. J. Am. Soc. Nephrol.* **10**, 1291–1299 (2015).
93. Kleiner, D. E. Recent advances in the histopathology of drug-induced liver injury. *Surg. Pathol. Clin.* **11**, 297–311 (2018).
94. Mendoza, M., Shotbolt, M., Faiq, M. A., Parra, C. & Chan, K. C. Advanced diffusion MRI of the visual system in glaucoma: from experimental animal models to humans. *Biology* **11**, 454 (2022).
95. Trivedi, V. et al. Widespread brain reorganization perturbs visuomotor coordination in early glaucoma. *Sci. Rep.* **9**, 14168 (2019).
96. Deng, W., Faiq, M. A., Liu, C., Adi, V. & Chan, K. C. Applications of manganese-enhanced magnetic resonance imaging in ophthalmology and visual neuroscience. *Front. Neural Circuits* **13**, 35 (2019).
97. Henriques, R. N., Henson, R., Cam-CAN & Correia, M. M. Unique information from common diffusion MRI models about white-matter differences across the human adult lifespan. *Imaging Neurosci.* **1**, 1–25 (2023).
98. Frishman, L. et al. ISCEV extended protocol for the photopic negative response (PhNR) of the full-field electroretinogram. *Doc. Ophthalmol.* **136**, 207–211 (2018).
99. Jnawali, A., Lin, X., Patel, N. B., Frishman, L. J. & Ostrin, L. A. Retinal ganglion cell ablation in guinea pigs. *Exp. Eye Res.* **202**, 108339 (2021).
100. Prencipe, M., Perossini, T., Brancoli, G. & Perossini, M. The photopic negative response (PhNR): measurement approaches and utility in glaucoma. *Int Ophthalmol.* **40**, 3565–3576 (2020).
101. Cone, F. E., Gelman, S. E., Son, J. L., Pease, M. E. & Quigley, H. A. Differential susceptibility to experimental glaucoma among 3 mouse strains using bead and viscoelastic injection. *Exp. Eye Res.* **91**, 415–424 (2010).
102. Chen, P. P. Correlation of visual field progression between eyes in patients with open-angle glaucoma. *Ophthalmology* **109**, 2093–2099 (2002).
103. Cooper, M. L. et al. Redistribution of metabolic resources through astrocyte networks mitigates neurodegenerative stress. *Proc. Natl. Acad. Sci. USA* **117**, 18810–18821 (2020).
104. Frankfort, B. J. et al. Elevated intraocular pressure causes inner retinal dysfunction before cell loss in a mouse model of experimental glaucoma. *Invest Ophthalmol. Vis. Sci.* **54**, 762–770 (2013).
105. Chen, H. et al. Commensal microflora-induced T cell responses mediate progressive neurodegeneration in glaucoma. *Nat. Commun.* **9**, 3209 (2018).
106. Bond, W. S. et al. Virus-mediated EpoR76E therapy slows optic nerve axonopathy in experimental glaucoma. *Mol. Ther.* **24**, 230–239 (2016).
107. Claes, M. et al. A fair assessment of evaluation tools for the murine microbead occlusion model of glaucoma. *Int. J. Mol. Sci*. **22**, 5633 (2021).
108. Creel, D. J., Dustman, R. E. & Beck, E. C. Visually evoked responses in the rat, guinea pig, cat, monkey, and man. *Exp. Neurol.* **40**, 351–366 (1973).
109. Woo, K. M., Guo, Y., Mehrabian, Z., Miller, N. R. & Bernstein, S. L. Refining flash visual evoked potential analysis in rats: a novel approach using bilateral epidural electrodes. *Transl. Vis. Sci. Technol.* **13**, 24–24 (2024).
110. Kruijt, C. C., de Wit, G. C., Talsma, H. E., Schalij-Delfos, N. E. & van Genderen, M. M. The detection of misrouting in albinism: evaluation of different VEP procedures in a heterogeneous cohort. *Invest Ophthalmol. Vis. Sci.* **60**, 3963–3969 (2019).
111. Porciatti, V. & Ventura, L. M. Retinal ganglion cell functional plasticity and optic neuropathy: a comprehensive model. *J. Neuroophthalmol.* **32**, 354–358 (2012).
112. Harwerth, R. S. et al. Visual field defects and neural losses from experimental glaucoma. *Prog. Retin Eye Res* **21**, 91–125 (2002).
113. Boia, R. et al. Neuroprotective strategies for retinal ganglion cell degeneration: current status and challenges ahead. *Int. J. Mol. Sci.* **21**, 2262 (2020).
114. Heo, H. J. et al. Mitochondrial pyruvate dehydrogenase phosphatase 1 regulates the early differentiation of cardiomyocytes from mouse embryonic stem cells. *Exp. Mol. Med.* **48**, e254–e254 (2016).
115. Fox, I. J. et al. Use of differentiated pluripotent stem cells in replacement therapy for treating disease. *Science* **345**, 1247391 (2014).
116. Bedel, A. et al. Preventing pluripotent cell teratoma in regenerative medicine applied to hematology disorders. *Stem Cells Transl. Med.* **6**, 382–393 (2017).

117. Yao, S. Q., Wang, M., Liang, J. J., Ng, T. K. & Cen, L. P. Retinal transcriptome of neonatal mice after optic nerve injury. *PLoS One* **18**, e0286344 (2023).
118. Wang, H. et al. Organization of a functional glycolytic metabolon on mitochondria for metabolic efficiency. *Nat. Metab.* **6**, 1712–1735 (2024).
119. Wei, Y. et al. Aerobic glycolysis is the predominant means of glucose metabolism in neuronal somata, which protects against oxidative damage. *Nat. Neurosci.* **26**, 2081–2089 (2023).
120. Lunt, S. Y. & Vander Heiden, M. G. Aerobic glycolysis: meeting the metabolic requirements of cell proliferation. *Annu Rev. Cell Dev. Biol.* **27**, 441–464 (2011).
121. Rangaraju, V., Calloway, N. & Ryan, T. A. Activity-driven local ATP synthesis is required for synaptic function. *Cell* **156**, 825–835 (2014).
122. Vlassenko, A. G. & Raichle, M. E. Brain aerobic glycolysis functions and Alzheimer's disease. *Clin. Transl. Imaging* **3**, 27–37 (2015).
123. Dienel, G. A. & Cruz, N. F. Aerobic glycolysis during brain activation: adrenergic regulation and influence of norepinephrine on astrocytic metabolism. *J. Neurochem.* **138**, 14–52 (2016).
124. Quistorff, B., Secher, N. H. & Van Lieshout, J. J. Lactate fuels the human brain during exercise. *FASEB J.* **22**, 3443–3449 (2008).
125. Feng, L. et al. Overexpression of brain-derived neurotrophic factor protects large retinal ganglion cells after optic nerve crush in mice. *eNeuro* **4**, ENEURO.0331–0316.2016 (2017).
126. Jiao, X., Peng, Y. & Yang, L. Minocycline protects retinal ganglion cells after optic nerve crush injury in mice by delaying autophagy and upregulating nuclear factor-κB2. *Chin. Med. J.* **127**, 1749–1754 (2014).
127. Zhou, X., Li, G., Zhang, S. & Wu, J. 5-HT1A receptor agonist promotes retinal ganglion cell function by inhibiting OFF-type presynaptic glutamatergic activity in a chronic glaucoma model. *Front. Cell Neurosci.* **13**, 167 (2019).
128. Zhou, X., Zhang, R., Zhang, S., Wu, J. & Sun, X. Activation of 5-HT1A receptors promotes retinal ganglion cell function by inhibiting the cAMP-PKA pathway to modulate presynaptic GABA release in chronic glaucoma. *J. Neurosci.* **39**, 1484–1504 (2019).
129. Wang, Y. et al. Muscle A-kinase anchoring protein-α is an injury-specific signaling scaffold required for neurotrophic- and cyclic adenosine monophosphate-mediated survival. *EBioMedicine* **2**, 1880–1887 (2015).
130. Chen, V. C. et al. Effects of selective serotonin reuptake inhibitors on glaucoma: a nationwide population-based study. *PLoS One* **12**, e0173005 (2017).
131. Calkins, D. J. Adaptive responses to neurodegenerative stress in glaucoma. *Prog. Retin Eye Res.* **84**, 100953 (2021).
132. Osborne, N. N. et al. 5-Hydroxytryptamine1A agonists: potential use in glaucoma. Evidence from animal studies. *Eye* **14**, 454–463 (2000).
133. Jöe, M. & Williams, P. A. Targeting Wallerian degeneration in glaucoma. *Neural Regen. Res.* **21**, 693–694 (2026).
134. Crish, S. D. & Calkins, D. J. Neurodegeneration in glaucoma: progression and calcium-dependent intracellular mechanisms. *Neuroscience* **176**, 1–11 (2011).
135. Gerdts, J., Brace, E. J., Sasaki, Y., DiAntonio, A. & Milbrandt, J. SARM1 activation triggers axon degeneration locally via NAD^+ destruction. *Science* **348**, 453–457 (2015).
136. Inman, D. M. & Harun-Or-Rashid, M. Metabolic vulnerability in the neurodegenerative disease glaucoma. *Front Neurosci.* **11**, 146 (2017).
137. Guo, X. et al. Preservation of vision after CaMKII-mediated protection of retinal ganglion cells. *Cell* **184**, 4299–4314.e4212 (2021).
138. Ross, A. G. et al. Rescue of retinal ganglion cells in optic nerve injury using cell-selective AAV mediated delivery of SIRT1. *Gene Ther.* **28**, 256–264 (2021).
139. Zuo, L. et al. SIRT1 promotes RGC survival and delays loss of function following optic nerve crush. *Invest Ophthalmol. Vis. Sci.* **54**, 5097–5102 (2013).
140. Xie, L., Yin, Y. & Benowitz, L. Chemokine CCL5 promotes robust optic nerve regeneration and mediates many of the effects of CNTF gene therapy. *Proc. Natl Acad. Sci. USA* **118**, e2017282118 (2021).
141. Zarei, K. et al. Automated axon counting in rodent optic nerve sections with axonJ. *Sci. Rep.* **6**, 26559 (2016).
142. Cone, F. E. et al. The effects of anesthesia, mouse strain and age on intraocular pressure and an improved murine model of experimental glaucoma. *Exp. Eye Res.* **99**, 27–35 (2012).

Acknowledgements

We thank the Hypoxia Core Facility at the Indiana University Cooperative Center for Excellence in Hematology (U54 DK106846) for Seahorse support, and Dr. Donald J. Zack for insightful feedback. Transmission-electron microscopy was performed with Derrick Gray, Dr. Quyen Q. Hoang, and Yangshin Park at the Indiana University School of Medicine (IUSM) Electron Microscopy Core; MRI sample preparation and imaging was assisted by Dr. Yu-Chien Wu and Erin E. Jarvis at the IU in vivo imaging core. We are thankful to Andi R. Masters and Christine M. Bach at the Clinical Pharmacology Analytical Core (CPAC, IUSM) for mass-spectrometry analyses, and to Drew M. Brown (Histology Core, IUSM) for tissue sectioning and H&E staining. We acknowledge Drs. Neha Mahajan, Qianyi Luo, and Ashay D. Bhatwadekar for OKR and ERG recordings; Drs. Amir R. Hajrasouliha and Sunland Gong for PhNR measurements; and Drs. Padmanabhan Pattabiraman and Avinash Soundararajan for IOP monitoring and anesthesia. Guidance in cryo-sectioning and staining was provided by Drs. Yoshikazu Imanishi, Sanae Imanishi, and Shimpei Takita; Dr. Weiming Mao for the access to his light-microscope; and Dr. Timothy W. Corson, Dr. Anbukkarasi Muniyandi, and Kamakshi Sishtla assisted with cell cycle analysis, enucleation and retinal dissection procedures. We thank Dr. Erica Cai (Indiana Biosciences Research Institute) for antisense-oligonucleotide (ASO) design, and Dr. Alyssa Coyne (Johns Hopkins University) for guidance on gymnotic ASO delivery. Drs. Thomas V. Johnson III and Erika A. Aguzzi (Johns Hopkins University) trained us optic-nerve crush and retinal flat-mount techniques; Dr. Harry A. Quigley and Elizabeth Kimball (Johns Hopkins University) assisted with the microbead glaucoma model. We thank Dr. Larry Benowitz and Dr. Yuqin Yin (Harvard Medical School) for providing the GAP-43 antibody, immunohistochemistry and image quantification protocols, and for reviewing GAP-43 positive optic nerve images. Funding was provided by the NIH (R00 EY028223 to A.D.; UL1 TR002529 to S.D. and A.D., R01 NS125020 to N.W.); Research to Prevent Blindness Challenge Grant to IU Ophthalmology, Indiana CTSI, The Glaucoma Foundation, Showalter Research Trust, Indiana University School of Medicine, and the BrightFocus Foundation (RReSTORe collaborative grant) to A. D. K.A. was supported in part by the Paul and Carole Stark Fellowship and a Sigma Xi Grant-in-Aid of Research. The content is solely the responsibility of the authors and does not necessarily represent the official views of the NIH.

Author contributions

A.D. conceived the study and supervised all aspects of the project. A.D., S.D., M.S., and K.A. designed the experiments, carried out the research, and analyzed the data. J.M. designed and executed the small-molecule screen. N.W. and J.C. processed, analyzed, and interpreted the MRI data.

Competing interests

The authors declare no competing interests. A.D. is an inventor on a patent application (PCT/US2024/044204) currently under review by the U.S. Patent and Trademark Office, filed through Indiana University School of Medicine.

Additional information

Supplementary information The online version contains supplementary material available at https://doi.org/10.1038/s43856-026-01528-3.

Correspondence and requests for materials should be addressed to Arupratan Das.

Peer review information *Communications Medicine* thanks Makoto Ishikawa, Richard Libby and the other, anonymous, reviewer(s) for their contribution to the peer review of this work. A peer review file is available.